Geochemical Indicators of the Peraluminous W-Cu-Mo-(±Sn-Li-Ta-Nb) Granites in Dahutang Orefield in Northern Jiangxi and Their Significance for Exploration

Haimin Ye *, Mangtin Shen *, Minggang Yu , Cunzhi Wang , Ling Zhao , Xilin Zhao

Posted Date: 14 October 2025

doi: 10.20944/preprints202510.0931.v1

Keywords: granite; geochemistry; W-Cu-Mo-(±-Sn-Li-Ta-Nb); mineralization; peraluminous; Dahutang orefield of Northern Jiangxi

Article

Geochemical Indicators of the Peraluminous W-Cu-Mo-(±Sn-Li-Ta-Nb) Granites in Dahutang Orefield in Northern Jiangxi and Their Significance for Exploration

Haimin Ye *, Mangtin Shen *, Mingang Yu, Cunzhi Wang, Ling Zhao and Xilin Zhao

Nanjing Institute of Geology and Mineral Resources, China Geological Survey, Nanjing 210016, Jiangsu, China

* Correspondence: 469907148@qq.com(H.Y.); smtq6483@sina.com(M.T.S.)

Abstract

The origin of Mesozoic granites associated with the Dahutang W-Cu-Mo orefield in north Jiangxi, which host the world's second largest tungsten deposit, remains a compelling subject despite extensive geochemical and geochronological studies. In this contribution we present new wolframite mineral and bulk-rock geochemistry and monazite U-Pb ages for the Mesozoic granites in aiming to enhance our understanding the petrogenesis of these granites and its coupling relationship with the mineralization. Two magmatic phases and four types of rocks in study area are identified, i.e., the early stage (152-147 Ma) biotite (G1) granite and the late stage (144-130 Ma) two-mica (G2)＋muscovite (G3)＋albite (G4) granite series. These two magmatic phases are temporally coincident with two mineralization stages (~150 Ma and 139-144 Ma). All the Mesozoic granites share the characteristics of high silica content, peraluminosity (A/CNK > 1.1), and low Zr+Nb+Ce+Y values (< 200 ppm), and they are derived from the partial melting of a Proterozoic crustal source. Specifically, the G1 granite, characterized by relatively high MgO (~0.5%), CaO (~1%), and low P_2O_5(0.13%-0.20%), is classified as an I-type granite. It formed via a relatively higher degree of partial melting at ~766°C (Zr saturation temperatures) driven by biotite breakdown reactions, with minor contributions from mantle-derived materials. In contrast, the G2–G4 granites series exhibits typical peraluminous S-type granite features, such as high Al_2O_3, Na_2O, and P_2O_5 (mostly >0.2%) contents, and low Sr and Ba contents. They are products of low-degree partial melting that occurred under conditions close to muscovite breakdown at ~735°C. Additionally, both granites show clear geochemical evidence of fluid interaction, as reflected by their elevated trace element and volatile contents: Sn>30 ppm, Cs >35 ppm, F >0.4%, Li >250 ppm, W 10–1000 ppm, Rb >500 ppm, K/Rb values <150, and Nb/Ta<5. The G1 granite represents a moderately fractionated melt relative to chondrites, as evidenced by its near-chondritic Zr/Hf (22.6-34.1) and Y/Ho (24.5-31.5) ratios, indicating a weaker influence of magmatic fluid-melt interaction. For the G2-G4 granites, however, intense crystal fractionation and late-stage fluid-melt interaction are well-documented by their highly variable and low ratios of Y/Ho (14.8-41.4), Nb/Ta (0.89-5.57), Zr/Hf (8.84-41.67), and K/Rb (13.96-128.29). In the long-lived, reduced, and volatile-rich aqueous environment of the G2–G4 magmas, fractional crystallization and albitization collectively enhanced the solubility and hydrothermal transport capacity of W, Sn, Li, Nb, and Ta by multiple orders of magnitude. In contrast, in the earlier, more oxidized G1 magma (which incorporated mantle materials), the exsolution and hydrothermal transport of Cu and Mo were associated with localized greisenization, but their capacity diminished with fractional crystallization. Historically, mineral exploration in the Dalutang mining area has focused primarily on W, Cu, and Mo. Based on this research, we conclude that there is significant mineral potential for rare metals (particularly Sn, Li, and Ta), and future surveys should prioritize areas adjacent to the evolved G2–G4 peraluminous leucogranites to search for new concealed mineral occurrences.

Keywords: granite; geochemistry; W-Cu-Mo-(±-Sn-Li-Ta-Nb); mineralization; peraluminous; Dahutang orefield of Northern Jiangxi

 doi:10.20944/preprints202510.0931.v1

1. Introduction

As the most evolved end members of granite series, rare-metal-bearing granites generally show remarkable enrichment in multiple high-value metallic elements including Li, Ta, Nb, W, Be and Sn. The study of rare-metal granites provides valuable insights into processes such as crustal growth, reworking events, thermal history, and fluid evolution during orogenic events [1, 2].

The Dahutang orefield, as the world's second largest W deposit, associated with Cu-Mo and rare metal mineralization (including Au, Ag, Sn, and so on), was identified in 2012 in northern Jiangxi Province, South China [3,4]. The genetically related Mesozoic peraluminous granites have subsequently attracted significant attentions owing to their considerable economic potential and scientific value. However, recognizing and characterizing these granites presents substantial challenges due to three primary factors: i) granites are mainly in a concealed state; ii) the local vegetation is luxuriant, which leads to most outcrops being concealed; and iii) they do not bear markedly distinctive petrophysical features, which hampers geophysical exploration.

Substantial research progress has been carried in understanding the petrogenesis and emplacement history of these granites, with notable achievements in rock geochemistry and isotope geochemistry studies. In particular, extensive investigations have been conducted on the multi-stage magmatic evolution and associated mineralization processes [5-13]. However, the genesis of the ore deposit and the ore-related granites remains debated, with controversies mainly focusing on: the spatiotemporal relationship between multi-stage granites and mineralization processes; the key characteristics of each stage of magmatism and mineralization; the co-existence mechanism of copper deposits and rare-metal mineralization.

This study integrates bulk-rock geochemical data of the petrographically well-characterized Mesozoic granites associated with W-Cu-Mo-(±Sn-Li-Ta-Nb) mineralization, along with monazite U-Pb ages, and wolframite mineral analyses. These data are applied to unravel the genesis and evolution of these granites, providing a comprehensive understanding of their origin and the relation with mineralization. This study offers new insights into the broader geological framework and mineral potential of the Dahutang ore cluster.

2. Geologic setting

2.1. Regional geology

The Dahutang polymetallic deposit in Northern Jiangxi (Figure1a) is located in the central segment of the Jiangnan Orogenic Belt, locally termed as the Jiuling Mountainswithin. The 1500-km-long ENE-WSW trending Jiangnan Orogenic belt lies along the southeastern margin of the Yangtze block (Figure 1). The Jiangnan Orogenic belt consists of Neoproterozoic arc terranes, which have experienced syn-schistose deformation and greenschist-facies metamorphism, culminating with the intrusion of Neoproterozoic granites (Jiuling granite; 819 Ma) [14,15]. The basement rocks of the Jiangnan Orogen are mainly Neoproterozoic metasedimentary and minor meta-volcanic rocks, known as the Shuangqiaoshan Group in this region.

Tectonically, the Dahutang ore cluster is bounded by the Jiujiang-Shitai and Jiangshan-Shaoxing faults (Figure 1). The region exhibits well-developed fault systems, including approximately W-E trending faults in the northern portion that intersect the Xin'anli tungsten deposit. Additionally, several NE-NNE trending faults are present (Figure 1b). The longest of these is the NNE-trending Xianguoshan- Shimensi- Shiweidong fault, extending over 25 km and hosting numerous ore deposits along its strike within the Dahutang district.

The meta-sedimentary sequence is the Neoproterozoic Shuangqiaoshan Group, a marine volcanic-clastic sedimentary succession comprising sandstones, phyllites, and slates interlayered with quartz-keratophyres and tuffs. The largest magmatic intrusion is the Jiuling Pluton, a

 doi:10.20944/preprints202510.0931.v1

Neoproterozoic granodiorite, emplaced as a batholith in Shuangqiaoshan Group.characterized by its It is gray in color and of coarse-grained texture and consists of medium- to coarse-grained biotite granodiorite. It is predominantly composed of plagioclase (65%), quartz (20%), and biotite (15%). The Jiuling Pluton contains numerous dark gray, deep-source xenoliths, typically rounded or elliptical in shape (with some irregular forms), ranging in size from several centimeters to tens of centimeters, and distributed sporadically throughout the intrusion.

Mesozoic intrusions occurr as small stocks, bosses, and sills, intrude into both the Neoproterozoic granodiorite and the Shuangqiaoshan Group.

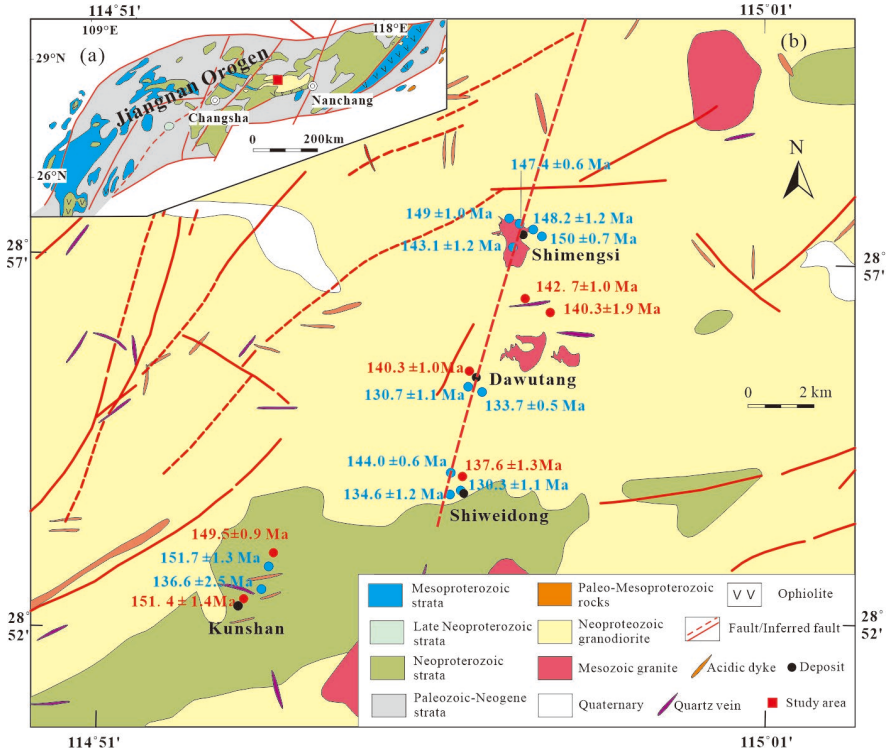

Figure 1. Geological sketch map of (a) the Jiangnan Orogen and (b) the Dahutang orefield. Age dta of the Mesozoic granites are denoted by symbols: red circle from this study data, blue circle from [5-7, 9, and 16].

2.2. Petrography of Mesozoic granites

Mesozoic granites, occurring as small stocks, bosses, and sills, emplaced into both the Neoproterozoic granodiorite and Shuangqiaoshan Group. The rock types closely associated with mineralization primarily include biotite granite, two-mica granite, and muscovite granite.

Biotite granite (G1) exhibits a porphyritic texture (Figure 2a), with a medium-grained monzonitic matrix. Phenocrysts predominantly comprise quartz (~3%), plagioclase (~6%), K-feldspar (~5%), and biotite (1%) with variable size. The matrix consists mainly of quartz (~35%), K-feldspar (~32%), plagioclase (~25%), biotite (~6%), muscovite (~2%), and minor magnetite. The rock has undergone intense greisenization, with irregular microcrystalline secondary quartz and sericite aggregates filling intergranular spaces, resulting in serrated edges on early-formed minerals. Plagioclase exhibits polysynthetic twinning or rhythmic zoning, with crystal edges showing a serrated shape due to fluid dissolution (Figure 2a).

Two-mica granite (G2) displays a massive structure and porphyritic texture, with phenocrysts dominated by plagioclase (~15%), K-feldspar (~10%), quartz (~10%), biotite (~3%), and muscovite (~2%). The matrix exhibits fine-grained texture (Figure 2b). Major mineral compositions include plagioclase (~15%), K-feldspar (~15%), quartz (~25%), muscovite (~3%), and minor biotite (1%), with accessory minerals such as ilmenite and magnetite. Quartz is found also as finer recrystallized crystals surrounding the rock constituting minerals (Figure 2b) which sometimes shows polygonal

 doi:10.20944/preprints202510.0931.v1

boundaries. K-feldspars are represented by coarse subhedral to anhedral tabular cystals of perthitic orthoclase with modest quantities of microcline. Biotite occurs as thick greenish brown to yellowish brown flakes and is replaced partially or completely by muscovite, chlorite and iron oxides. Sericite is found as irregular aggregates replaces K-feldspar, biotite and is replaced by chlorite and opaque minerals (Figure 2c).

The muscovite granite (G3) exhibits distinct zoning structure. From the outer to the inner portions of the rock-mass contact zone, it can be subdivided into fine-grained → medium-grained → coarse-grained muscovite granite. The fine-grained muscovite granite shows strong mineralization, particularly Li mineralization, serving as the primary ore-hosting rock in the mining area. In contrast, the medium- to coarse-grained muscovite granite distal to the contact zone displays poor mineralization. The rock is grayish-white to flesh-red in color and composed of quartz (~40%), plagioclase (~30%), K-feldspar (~25%), muscovite (11-15%), and trace biotite (~2%) (Figure 2d). The fine-grained muscovite granite has undergone intense albitization, as evidenced by the nearly complete replacement of K-feldspar by albite and muscovite, the predominant alteration of plagioclase into albite, and the common occurrence of Li-mica bordering and replacing the margins of muscovite (Figure 2d). Lithium is predominantly hosted in Li-mica. The local fine-grained muscovite granite gradually transitions, instead of a distinct interface, into albite granite (G4).

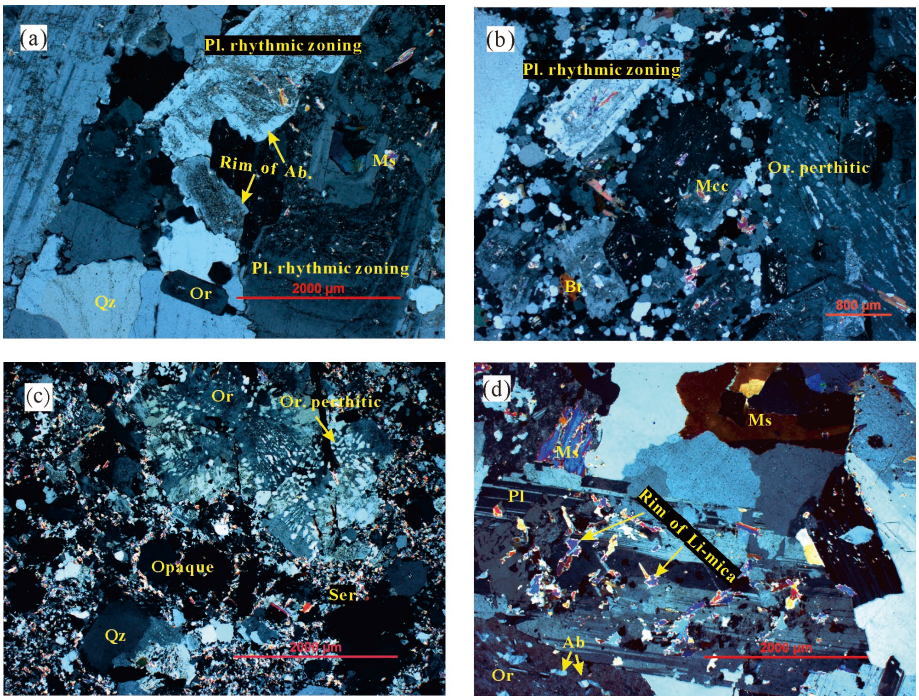

Figure 2. Microphotographs (crossed polarizers) of the Dahutang orefield. (a) Biotite (G1) granite. Plagioclase exhibits polysynthetic twinning or rhythmic zoning, with crystal edges showing a serrated shape due to fluid dissolution; (b) Two-mica (G2) granite. Coarse quartz and plagioclase surrounded by fine recrystallized quartz along its boundaries. Orthoclase perthite crystal shows patch perthite type; (c) Two-mica granite. Sericite aggregates replaces K-feldspar, biotite and is replaced by chlorite and opaque minerals; (d) Muscovite granite. Margins of muscovite are bordered and replaced by Li-mica. (Pl= plagioclase; Or= orthoclase; Mcc= microcline; Ms=muscovite; Qz=quartz; Bt=biotite; Ab= albite; Ser=Sericite).

3. Ore characteristics

Fifteen large, medium, and small mineral deposits and ore occurrences have been identified in the Dahutang and its marginal area, forming a significant ore concentration zone dominated by W associated with Cu, Mo, Li, Sn, Nb, Ta, and other rare metals. The region hosts a resource of 1.1×10^6 t of WO_3, accompanied by 0.65×10^6 t Cu and 28000t Mo. Multiple large-to-medium-sized W-Cu-Mo

 doi:10.20944/preprints202510.0931.v1

polymetallic deposits are distributed across the area, including the Shimensi, Dawutang, Shiweidong, and Kunshan mining areas (Figure 1b).

Orefield mainly comprise four genetic types: disseminated vein type, altered granite type, hydrothermal cryptoexplosive breccia type, and large quartz vein type (Figure 3). Among these, the former two types are the most economically important and exhibit typical porphyry-style characteristics, including pervasive whole-rock alteration-mineralization, low-grade mineralization, and large-tonnage deposit scales. The industrial W ore types: Scheelite dominant ores with minor wolframite and sulfides in the disseminated-veinlet and altered granite, and wolframite dominant ores with minor scheelite and sulfide in the quartz vein.

Disseminated-veined and altered-granite ores occur in the contact zones between Mesozoic granites and Neoproterozoic biotite granodiorite (Figures 3a, b). These ores generally dip gently, typically at 10°-30°, largely concurrent with the orientation of the contacting surfaces. These type ores are well-developed in the Shimensi and Dawutang mining areas. Disseminated-veined ores that distribute within the exocontact zones (the Neoproterozoic granodiorite) are the most important type in the mining area (Figure 3 and Figure 4a, b), and exhibit higher grade and better mineralization continuity, whereas those in the endocontact zone are generally thinner, lower-grade, and show discontinuous mineralization. Hydrothermal alteration associated with disseminated-vein type ores is extensive, with greisen alteration being the major type. The altered-granite type ores occurs in the cupolas of the muscovite granite and albite granite the (Figure 3b). Potassic alteration and albite alteration is the dominant alteration type associated with altered-granite type ores (Figure 2d). These two type ores share similar strikes and geometries, often coexist or occur independently. Major ore minerals include scheelite, wolframite, chalcopyrite, lepidolite, zinnwaldite, and molybdenite.

Hydrothermal cryptoexplosive breccia type ores are mainly distributed in the upper parts of Mesozoic granite intrusions, with ores orientations perpendicular to the intrusive contact surfaces (Figure 3a). The breccia matrix consists of magma melt or felsic hydrothermal materials, while breccia are predominantly Neoproterozoic granodiorite, with minor Mesozoic granite (Figures 4e). These ore bodies exhibit complex morphologies, with type ores dominated by veinlet-disseminated ores. Ore assemblages are intricate and diverse, with primary metallic minerals including wolframite, scheelite, chalcopyrite, and molybdenite, followed by stannite, sphalerite, cassiterite, and others.

Quartz-vein type ores are primarily hosted within Neoproterozoic granodiorite and Shuangqiaoshan Group (Figure 4g, h), and its occurrence is mainly controlled by fracture structures. This type ores are commonly seen in the Shimensi, Shiweidong, and Kunshan mining areas. This type of ores has the highest W average grade of 0.282% and accounts for about 1% of the total W resource. Wolframite is also the main ore mineral, and scheelite is the second. Wolframite occurs as coarse tabular or columnar crystals along the walls of large veins, with long axes growing perpendicular or oblique to the vein walls, forming symmetrical comb structures (Figure 4g). Associated metallic minerals primarily include molybdenite (Figure 4i) and chalcopyrite.

 doi:10.20944/preprints202510.0931.v1

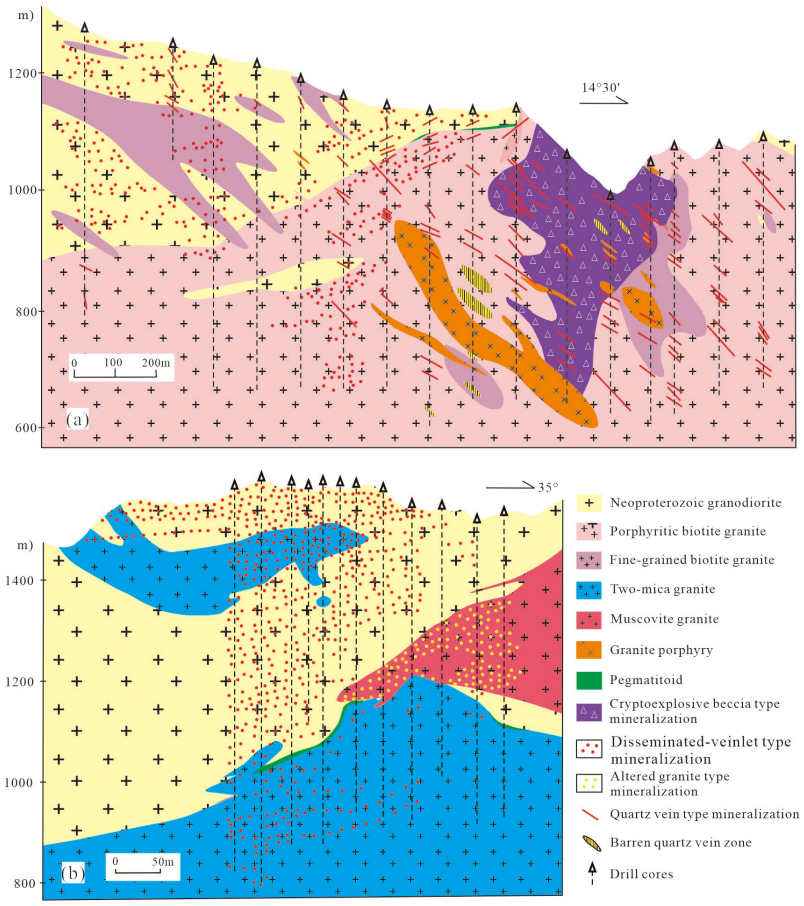

Figure 3. Geological section along (a) the No. 4 exploration line of the Shimensi mining area, and (b) the No.6 exploration of the Dawutang mining area. Compiled and redrawn based on [17,18].

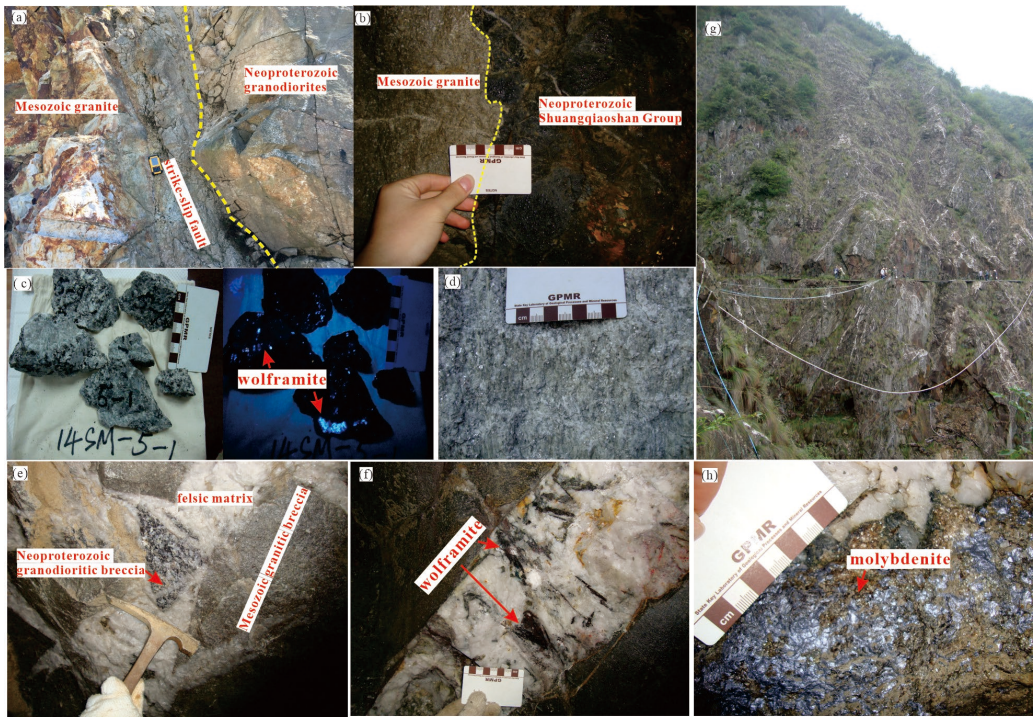

Figure 4. Field photographs of rocks and ores of the Dahutang orefield. (a) Mesozoic granite intrudes into Neoproterozoic granodiorite; (b) Mesozoic granite intrudes into Neoproterozoic Shuangqiaoshan Group; (c)

 doi:10.20944/preprints202510.0931.v1

Disseminated-veinlet tungsten ore; (d) altered-granite type ore; (e) Hydrothermal cryptoexplosive breccia; (f) Comb-like wolframite aggregates growing vertically or obliquely to the vein walls; (g) crisscrossing quartz veinlets in the Kunshan mining area; (i) Scaly molybdenite.

4. Materials and Methods

4.1. minerals collection

Wolframite, monazite, and zircon minerals were sourced from the Mesozoic granites of the Dahutang orefield (Table 1). These minerals were separated from the samples using the heavy mineral separation method, and homogeneous, transparent grains were selected under a binocular microscope to prepare sample mounts. 22 samples were collected for whole-rock chemical analyses from the Shimensi mining area, the Kunshan mining area and the Dawutang mining area.

Table 1. Summary of minerals analyzed in the study area.

Sample	mining section	lithology	mineral	analysis
SM-34	Shimengsi mining area	Biotite granite (G1)	wolframite	EMPA major element analysis
14SWD-1	Shiweidong mining area	Two-mica granite (G2)	wolframite	EMPA major element analysis
			monazite	LA-ICP-MS U-Pb dating
14PM-5	Dawutang mining area	Moscovite granite (G3)	monazite	LA-ICP-MS U-Pb dating
14PM-8	Dawutang mining area	Porphyry two-mica granite（G2）	zircon	LA-ICP-MS U-Pb dating
14YKD-1	Dawutang mining area	Two-mica granite(G2)	wolframite	EMPA major element analysis
			monazite	LA-ICP-MS U-Pb dating
14YSD-3-1	Kunshan mining area	Biotite granite (G1)	wolframite	EMPA major element analysis
			monazite	LA-ICP-MS U-Pb dating
14YSD-3-2	Kunshan mining area	Biotite granite (G1）	monazite	LA-ICP-MS U-Pb dating

4.2. Back-Scaterred Electron of wolframite

The targets and Back-Scaterred Electron (BSE) photographs of wolframite, monazite, and zircon were conducted at the Institute of Geology and Geophysics, Chinese Academy of Sciences. The major elements analyses of wolframite were conducted at the Institute of Geology and Geophysics, Chinese Academy of Sciences by the JXA-8100 electron probe with a excitation voltage of 20 KV, a excitation current of 1×10^{-8} A and a spot size of 0.5 μm.

4.3. Laser ablation ICP-MS of monazite and zircon

The U-Pb dating analyses of monazite and zircon was carried at the isotope Laboratory of Tianjin Geological Survey Center of China Geological Survey by the laser ablation Multi-receiving Plasma mass spectrometer (LA-ICP-MS), with using an excimer laser of NEW WAVE 193 nm FX ArF, a NEPUNE multi-receiver inductively coupled plasma mass spectrometer. Each analysis consisted of 20~30s of background signal acquisition followed by 65s of ablation. During sample analysis, monazite standard sample 44,069 and zircon GJ-1 were used as the external age standard for U-Pb isotopic fractionation correction. In the standard deviation of the standard of isotope ratio, the standard deviation of the isotope ratio of the sample and the standard isotope ratio is also taken into account, and the relative standard deviation is set at 2%. Isotopic age mapping was performed using the ISOPLOT/EX 3.23 procedure [19]. Data without common Pb correction are plotted on the Tera-Wasserburg diagram. The $^{206}Pb/^{238}U$ age was calculated as a lower intercept of the $^{206}Pb/^{238}U$ value of the regression line with the Concordia curve. Weighted mean ages for each spot were calculated using the ^{207}Pb-correction for common Pb.

4.4. whole-rock chemical analyses

 doi:10.20944/preprints202510.0931.v1

In this paper, Whole-rock major- and trace-element analyses were carried out at the analysis and test Center of Nanjing Geological Survey Center of China Geological Survey. Fresh samples were crushed and powdered in an agate grinder mill and sieved with a < 200 μm mesh. Major elements were analyzed as a fused disk using X-ray fluorescence (XRF) spectroscopy (PANalytical PW2424) with measurement uncertainty standard deviation of <5 %. LOI at 1000℃ was measured for each sample, and elemental concentrations were normalized with the results of both analyses. Rare earth and other trace elements were analyzed using a Perkin Elmer Elan 9000 inductively coupled plasma-mass spectroscopy (ICP-MS) in solution mode. Prepared samples were added to lithium metaborate/lithium tetraborate flux, mixed well and fused in a furnace at 1025℃. The resulting melts were then cooled and dissolved in a mixture of nitric, hydrochloric and hydrofluoric acids prior to analysis. Standards were used to monitor the reliability of analytical results, and accuraccy were 1~5 % for major elements and 5~10 % for most trace elements.

5. Results

5.1. Geochronology

5.1.1. Dawutang mining area

Monazites from the medium- to coarse-grained G3 granite (14PM-5) and fine-grained G2 granite (14YKD-1) are light yellow, subhedral to euhedral, with grain sizes ranging from 50 to 80 μm. Under back-scattered electron (BSE) images, their structures are relatively homogeneous, with indistinct zoning (Figure 5). A total of 28 and 29 analytical points were acquired for 14PM-5 and 14YKD-1, respectively. Data were plotted and calculated on Tera-Wasserburg inverse concordia diagrams. For 14PM-5, the monazite lower intercept age is 142.9±1.0 Ma (MSWD=2.3), with a weighted mean $^{206}Pb/^{238}U$ age of 142.7±1.0 Ma (MSWD=1.1). For 14YKD-1, the monazite lower intercept age is 139.2±0.98 Ma (MSWD=1.3), and the weighted mean $^{206}Pb/^{238}U$ age is 140.6±1.3 Ma (MSWD = 0.52) (Figure 6, Table 2).

Zircons from the porphyritic G2 granite (14PM-8) are elongated, subhedral to euhedral, with grain sizes varying from 50 to 100 μm. Under cathodoluminescence (CL) imaging, zircons are dark in color, displaying zoning, and some grains exhibit core-rim structures with bright cores and dark black rims. A total of 16 zircon grains from 14PM-8 were analyzed, but data from 7 grains with U>10,000 ppm and obvious inherited characteristics were excluded from plotting and calculations. Measured $^{207}Pb/^{206}Pb$ and $^{206}Pb/^{238}U$ values (without common Pb correction) were plotted on a Tera-Wasserburg inverse concordia diagram, and the weighted mean $^{206}Pb/^{238}U$ age was calculated. Results yield a lower intercept age of 140.0±1.4 Ma (MSWD=1.6) and a weighted mean age of 140.3±1.9 Ma (MSWD = 0.43) (Figure 6, Table 2).

5.1.2. Shiweidong mining area

The monazites from the G2 granite (14SWD-1) are light yellow, euhedral to subhedral crystals ranging from 60 to 90 μm in size. Backscattered electron (BSE) imaging reveals a uniform internal structure with indistinct zoning (Figure 5). Thirty analyses of these monazites yield a lower intercept age of 137.6 ± 1.3 Ma (MSWD=3.0) and a weighted average $^{206}Pb/^{238}U$ age of 137.5 ± 1.0 Ma (MSWD=0.72) (Figure 6, Table 2).

5.1.3. Kunshan mining area

The monazites from two G1 granite samples (14YSD-3-1, 14YSD-3-2) are colorless, transparent, subhedral columnar crystals measuring 80-150 μm, displaying distinct banding under backscattered electron (BSE) imaging (Figure 5). Thirty-two analyses of monazites from 14YSD-3-1 yield a lower intercept age of 149.6±0.6 Ma (MSWD=0.8) and a weighted mean $^{206}Pb/^{238}U$ age of 149.5±0.9 Ma (MSWD = 0.3). Thirty-one analyses of monazites from 14YSD-3-2 yield a lower intercept age of

 doi:10.20944/preprints202510.0931.v1

151.8±1.5 Ma (MSWD = 0.7) and a weighted average $^{206}Pb/^{238}U$ age of 151.4±1.4 Ma (MSWD = 1.2; Figure 6, Table 2).

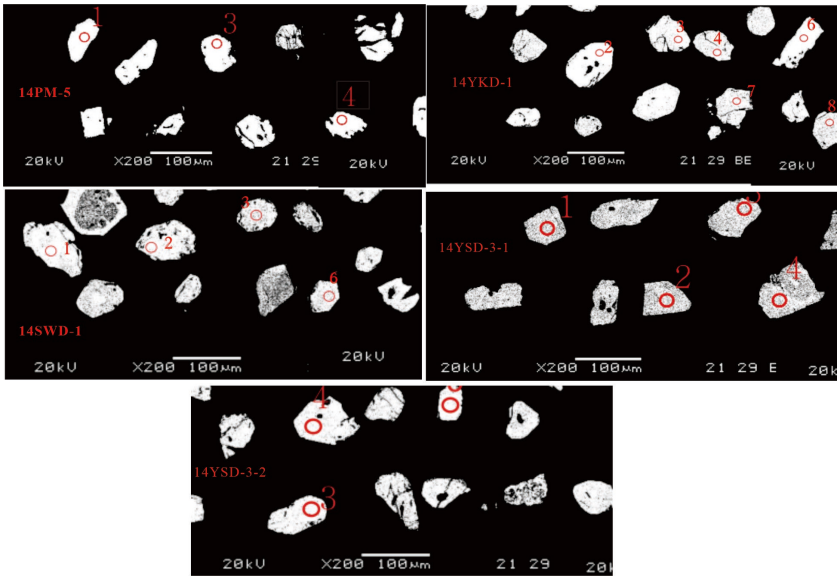

Figure 5. Representative Back-Scaterred Electron (BSE) images of monazite grains used for U–Pb dating.

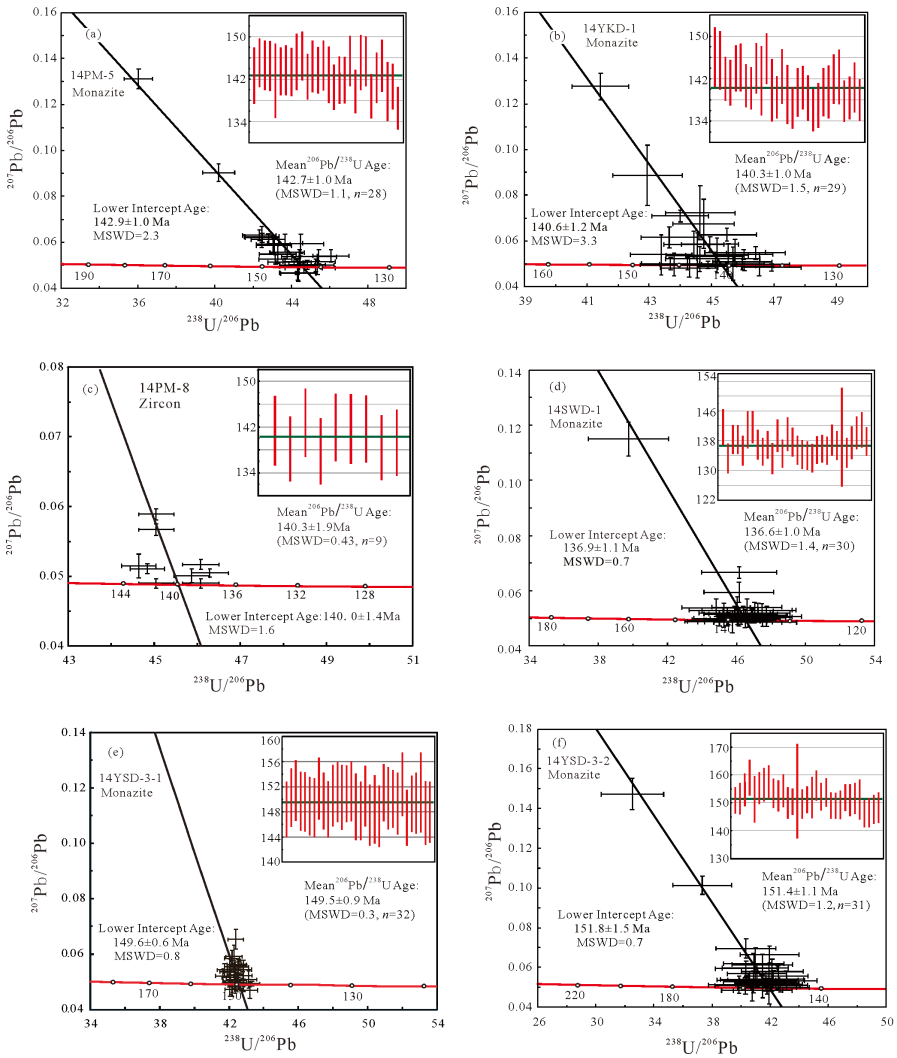

 doi:10.20944/preprints202510.0931.v1

Figure 6. Tera-Wasserburg (T-W) Concordia diagrams and ^{207}Pb-corrected weighted mean $^{206}Pb/^{238}U$ ages of monazites from Mesozoic granite in the Dawutang, Shiweidong and Kunshan mining area.

Table 2. LA-ICP-MS monazite and zircon U-Pb analysis data of Mesozoic granites in the Dahutang District.

Mineral/sample	Isotope ratios ($^{207}Pb/^{206}Pb$ =0.461±0.02)						Age, Ma	
monazite/14PM-5 (Dawutang mining area)	$^{206}Pb/^{238}U$	1σ	$^{207}Pb/^{235}U$	1σ	$^{207}Pb/^{206}Pb$	1σ	$^{206}Pb/^{238}U$	1σ
1	0.0249	0.0003	0.3097	0.0081	0.0903	0.0018	143	2
3	0.0229	0.0002	0.1617	0.0037	0.0512	0.0008	145	2
5	0.0226	0.0002	0.1452	0.0052	0.0467	0.0015	145	2
6	0.0234	0.0002	0.1970	0.0049	0.0612	0.0012	144	2
7	0.0278	0.0003	0.5021	0.0111	0.1312	0.0021	142	2
8	0.0226	0.0002	0.1554	0.0048	0.0500	0.0013	143	2
9	0.0226	0.0002	0.1540	0.0061	0.0495	0.0018	144	2
10	0.0228	0.0002	0.1752	0.0055	0.0556	0.0015	143	2
11	0.0236	0.0003	0.2027	0.0084	0.0624	0.0023	145	2
12	0.0232	0.0002	0.1680	0.0040	0.0526	0.0010	146	2
14	0.0225	0.0002	0.1600	0.0043	0.0516	0.0012	142	2
16	0.0232	0.0002	0.1894	0.0067	0.0592	0.0019	144	2
17	0.0227	0.0002	0.1601	0.0041	0.0512	0.0011	144	2
18	0.0225	0.0002	0.1443	0.0057	0.0464	0.0017	145	2
19	0.0224	0.0002	0.1509	0.0042	0.0489	0.0011	143	2
20	0.0221	0.0002	0.1522	0.0047	0.0500	0.0014	140	2
21	0.0225	0.0002	0.1670	0.0050	0.0538	0.0014	142	2
22	0.0223	0.0002	0.1543	0.0039	0.0502	0.0010	142	2
23	0.0236	0.0002	0.2053	0.0049	0.0630	0.0012	145	2
24	0.0220	0.0002	0.1569	0.0044	0.0516	0.0012	140	1
25	0.0231	0.0003	0.1746	0.0071	0.0548	0.0021	145	2
26	0.0235	0.0002	0.2011	0.0044	0.0620	0.0010	145	2
27	0.0220	0.0002	0.1629	0.0053	0.0537	0.0015	139	2
28	0.0229	0.0002	0.1877	0.0067	0.0595	0.0019	142	2
29	0.0232	0.0002	0.1871	0.0063	0.0585	0.0017	144	2
30	0.0225	0.0003	0.1838	0.0082	0.0593	0.0021	140	2
31	0.0220	0.0002	0.1486	0.0049	0.0489	0.0014	141	2
32	0.0217	0.0002	0.1618	0.0048	0.0541	0.0014	136	1
Mineral/sample	**Isotope ratios ($^{207}Pb/^{206}Pb$ =0.91±0.09)**						**Age, Ma**	
monazite/14YKD-1 (Dawutang mining area)	$^{206}Pb/^{238}U$	1σ	$^{207}Pb/^{235}U$	1σ	$^{207}Pb/^{206}Pb$	1σ	$^{206}Pb/^{238}U$	1σ
1	0.0230	0.0003	0.1713	0.0141	0.0539	0.0044	146	2
2	0.0228	0.0003	0.1558	0.0085	0.0495	0.0025	145	2
3	0.0223	0.0002	0.1518	0.0034	0.0494	0.0008	142	1
4	0.0227	0.0002	0.2220	0.0052	0.0709	0.0013	141	2
5	0.0226	0.0002	0.1556	0.0048	0.0499	0.0014	144	2
6	0.0226	0.0002	0.1497	0.0069	0.0481	0.0021	144	2
7	0.0222	0.0002	0.1622	0.0038	0.0531	0.0010	141	1
8	0.0220	0.0002	0.1484	0.0033	0.0490	0.0008	140	1
9	0.0229	0.0002	0.1943	0.0078	0.0615	0.0023	144	2
10	0.0233	0.0003	0.2844	0.0219	0.0886	0.0066	142	2
11	0.0229	0.0002	0.1579	0.0048	0.0500	0.0013	146	2
12	0.0241	0.0003	0.4246	0.0115	0.1276	0.0029	140	2
13	0.0217	0.0002	0.1467	0.0036	0.0490	0.0010	138	1

 doi:10.20944/preprints202510.0931.v1

15	0.0224	0.0003	0.1607	0.0088	0.0520	0.0027	142	2
16	0.0224	0.0003	0.2231	0.0182	0.0722	0.0059	139	2
17	0.0215	0.0002	0.1627	0.0049	0.0548	0.0014	136	1
18	0.0219	0.0002	0.1510	0.0112	0.0500	0.0036	139	2
19	0.0222	0.0002	0.1794	0.0059	0.0585	0.0017	140	1
20	0.0219	0.0002	0.1654	0.0091	0.0549	0.0029	138	2
21	0.0213	0.0002	0.1420	0.0032	0.0483	0.0008	136	1
22	0.0215	0.0002	0.1474	0.0080	0.0497	0.0026	137	2
23	0.0220	0.0002	0.1580	0.0104	0.0522	0.0033	139	2
24	0.0223	0.0002	0.2078	0.0171	0.0674	0.0054	139	2
25	0.0225	0.0002	0.1811	0.0096	0.0584	0.0030	142	2
27	0.0224	0.0003	0.1659	0.0155	0.0536	0.0049	142	2
28	0.0217	0.0002	0.1619	0.0039	0.0541	0.0010	138	1
30	0.0217	0.0002	0.1522	0.0055	0.0507	0.0017	138	1
31	0.0221	0.0002	0.1638	0.0121	0.0537	0.0038	140	2
32	0.0220	0.0002	0.1899	0.0052	0.0627	0.0014	138	1

Mineral/sample	Content (ppm)		Isotope ratios						Age, Ma	
zircon/14PM-8 (Dawutang mining area)	Th	U	$^{206}Pb/^{238}U$	1σ	$^{207}Pb/^{235}U$	1σ	$^{207}Pb/^{206}Pb$	1σ	$^{206}Pb/^{238}U$	1σ
1	141	2190	0.0222	0.0002	0.1497	0.0023	0.0490	0.0007	141	2
6	191	2734	0.0217	0.0002	0.1546	0.0022	0.0517	0.0007	138	1
7	393	574	0.0224	0.0002	0.1589	0.0054	0.0515	0.0017	143	1
8	113	5484	0.0216	0.0002	0.1503	0.0022	0.0505	0.0006	138	1
9	236	4014	0.0223	0.0002	0.1569	0.0023	0.0511	0.0007	142	1
10	1061	6327	0.0222	0.0002	0.1738	0.0026	0.0567	0.0008	142	2
11	99	5639	0.0222	0.0002	0.1805	0.0028	0.0589	0.0008	142	1
15	33	1722	0.0217	0.0002	0.1466	0.0023	0.0490	0.0007	138	1
16	81	1276	0.0218	0.0002	0.1510	0.0032	0.0501	0.0010	139	1

Mineral/sample	Isotope ratios ($^{207}Pb/^{206}Pb$ =0.542±0.093)						Age, Ma	
monazite/14SWD-1 (Shiweidong mining area)	$^{206}Pb/^{238}U$	1σ	$^{207}Pb/^{235}U$	1σ	$^{207}Pb/^{206}Pb$	1σ	$^{206}Pb/^{238}U$	1σ
1	0.0222	0.0002	0.1494	0.0032	0.0488	0.0008	142	2
2	0.0217	0.0002	0.1990	0.0045	0.0666	0.0010	133	1
3	0.0217	0.0002	0.1475	0.0032	0.0493	0.0008	138	1
4	0.0217	0.0002	0.1456	0.0031	0.0487	0.0007	138	1
6	0.0217	0.0002	0.1773	0.0061	0.0593	0.0018	135	1
7	0.0223	0.0002	0.1655	0.0056	0.0538	0.0016	141	2
8	0.0220	0.0002	0.1513	0.0041	0.0499	0.0011	140	2
9	0.0215	0.0002	0.1474	0.0053	0.0497	0.0016	137	1
10	0.0212	0.0002	0.1470	0.0032	0.0502	0.0008	135	1
11	0.0214	0.0002	0.1431	0.0032	0.0484	0.0008	137	1
12	0.0209	0.0002	0.1463	0.0057	0.0507	0.0018	133	2
13	0.0218	0.0002	0.1467	0.0062	0.0487	0.0019	139	2
14	0.0212	0.0002	0.1471	0.0031	0.0504	0.0008	134	1
15	0.0221	0.0002	0.1609	0.0046	0.0528	0.0013	140	2
16	0.0217	0.0002	0.1541	0.0036	0.0515	0.0009	138	1
17	0.0215	0.0002	0.1598	0.0051	0.0540	0.0015	135	1
18	0.0210	0.0002	0.1407	0.0031	0.0485	0.0008	134	1
19	0.0212	0.0002	0.1544	0.0044	0.0529	0.0013	134	1
20	0.0211	0.0002	0.1535	0.0041	0.0529	0.0012	133	1
21	0.0213	0.0002	0.1496	0.0039	0.0509	0.0011	135	1

 doi:10.20944/preprints202510.0931.v1

22	0.0213	0.0002	0.1474	0.0034	0.0501	0.0009	136	1
23	0.0213	0.0002	0.1496	0.0043	0.0510	0.0013	135	1
24	0.0218	0.0002	0.1558	0.0045	0.0519	0.0013	138	1
25	0.0216	0.0002	0.1531	0.0047	0.0515	0.0014	137	1
26	0.0252	0.0003	0.3988	0.0139	0.1150	0.0031	139	5
27	0.0213	0.0002	0.1524	0.0059	0.0520	0.0018	135	1
28	0.0217	0.0002	0.1577	0.0082	0.0527	0.0026	137	2
29	0.0220	0.0002	0.1504	0.0043	0.0496	0.0012	140	2
31	0.0221	0.0002	0.1492	0.0043	0.0490	0.0012	141	2
32	0.0216	0.0002	0.1470	0.0032	0.0493	0.0008	138	1

Mineral/sample	**Isotope ratios ($^{207}Pb/^{206}Pb$ =0.84±0.12)**						**Age, Ma**	
monazite/14YSD-3-1 (Kunshan mining area)	**$^{206}Pb/^{238}U$**	**1σ**	**$^{207}Pb/^{235}U$**	**1σ**	**$^{207}Pb/^{206}Pb$**	**1σ**	**$^{206}Pb/^{238}U$**	**1σ**
1	0.0235	0.0002	0.1803	0.0062	0.0557	0.0017	148	1
2	0.0236	0.0002	0.1605	0.0073	0.0493	0.0021	150	2
3	0.0237	0.0002	0.1544	0.0082	0.0472	0.0024	151	2
4	0.0236	0.0002	0.1705	0.0079	0.0524	0.0023	150	2
5	0.0235	0.0002	0.1636	0.0044	0.0505	0.0011	150	2
6	0.0234	0.0002	0.1570	0.0078	0.0487	0.0023	149	2
7	0.0235	0.0002	0.1814	0.0089	0.0559	0.0026	149	2
8	0.0240	0.0002	0.1796	0.0079	0.0544	0.0023	152	2
9	0.0235	0.0002	0.1595	0.0067	0.0492	0.0019	150	2
10	0.0235	0.0002	0.1820	0.0068	0.0562	0.0019	148	2
11	0.0238	0.0002	0.1750	0.0091	0.0534	0.0027	151	2
12	0.0238	0.0002	0.1649	0.0068	0.0503	0.0019	151	2
13	0.0236	0.0003	0.1654	0.0112	0.0508	0.0033	150	2
14	0.0237	0.0002	0.1616	0.0049	0.0495	0.0013	151	2
15	0.0239	0.0002	0.1765	0.0066	0.0536	0.0018	151	2
16	0.0236	0.0003	0.1926	0.0143	0.0591	0.0042	149	2
17	0.0234	0.0002	0.1787	0.0085	0.0553	0.0025	148	2
18	0.0236	0.0002	0.1582	0.0091	0.0486	0.0027	151	2
19	0.0232	0.0002	0.1624	0.0101	0.0508	0.0031	147	2
20	0.0234	0.0003	0.1681	0.0057	0.0522	0.0016	148	2
21	0.0236	0.0002	0.2125	0.0119	0.0653	0.0035	147	2
22	0.0237	0.0002	0.1629	0.0044	0.0498	0.0011	151	2
23	0.0236	0.0002	0.1617	0.0102	0.0497	0.0030	150	2
24	0.0235	0.0002	0.1578	0.0049	0.0486	0.0013	150	2
25	0.0237	0.0003	0.1912	0.0097	0.0585	0.0028	149	2
26	0.0240	0.0002	0.1726	0.0092	0.0522	0.0026	152	2
27	0.0231	0.0002	0.1571	0.0035	0.0494	0.0008	147	2
28	0.0236	0.0002	0.1832	0.0059	0.0562	0.0016	149	2
29	0.0236	0.0002	0.1772	0.0098	0.0544	0.0029	149	2
30	0.0238	0.0003	0.1690	0.0216	0.0515	0.0067	151	2
31	0.0233	0.0003	0.1751	0.0114	0.0544	0.0034	148	2
32	0.0231	0.0002	0.1499	0.0099	0.0470	0.0030	148	2

Mineral/sample	**Isotope ratios ($^{207}Pb/^{206}Pb$ =0.509±0.052)**						**Age, Ma**	
monazite/14YSD-3-2 (Kunshan mining area)	**$^{206}Pb/^{238}U$**	**1σ**	**$^{207}Pb/^{235}U$**	**1σ**	**$^{207}Pb/^{206}Pb$**	**1σ**	**$^{206}Pb/^{238}U$**	**1σ**
1	0.0238	0.0002	0.1716	0.0048	0.0522	0.0012	151	2
2	0.0245	0.0003	0.2090	0.0093	0.0620	0.0025	151	2
3	0.0245	0.0003	0.1784	0.0096	0.0529	0.0027	155	2
4	0.0251	0.0003	0.1774	0.0081	0.0513	0.0022	159	2

 doi:10.20944/preprints202510.0931.v1

5	0.0268	0.0003	0.3739	0.0103	0.1013	0.0022	151	3
6	0.0246	0.0003	0.1832	0.0073	0.0540	0.0020	155	2
7	0.0245	0.0003	0.1638	0.0093	0.0485	0.0026	156	2
8	0.0248	0.0003	0.1743	0.0077	0.0509	0.0021	157	2
9	0.0243	0.0002	0.1798	0.0066	0.0536	0.0018	153	2
10	0.0243	0.0003	0.1908	0.0093	0.0569	0.0026	152	2
11	0.0248	0.0003	0.2032	0.0076	0.0595	0.0020	154	2
12	0.0237	0.0003	0.1745	0.0088	0.0533	0.0025	150	2
13	0.0238	0.0002	0.1766	0.0055	0.0537	0.0015	150	2
14	0.0308	0.0003	0.6241	0.0196	0.1472	0.0039	154	5
15	0.0241	0.0003	0.2045	0.0091	0.0615	0.0025	149	2
16	0.0238	0.0002	0.1659	0.0049	0.0506	0.0012	151	2
17	0.0244	0.0003	0.2012	0.0168	0.0598	0.0050	152	2
18	0.0248	0.0002	0.1833	0.0050	0.0537	0.0012	156	2
19	0.0239	0.0002	0.1647	0.0061	0.0499	0.0017	152	2
20	0.0241	0.0002	0.1611	0.0066	0.0485	0.0018	154	2
21	0.0235	0.0002	0.1657	0.0041	0.0512	0.0010	149	2
22	0.0234	0.0002	0.1611	0.0043	0.0499	0.0011	149	2
23	0.0237	0.0002	0.1766	0.0078	0.0541	0.0022	149	2
24	0.0240	0.0002	0.1735	0.0044	0.0524	0.0010	152	2
25	0.0248	0.0003	0.2378	0.0091	0.0696	0.0024	151	2
26	0.0240	0.0003	0.1753	0.0087	0.0530	0.0025	152	2
28	0.0238	0.0003	0.1696	0.0165	0.0516	0.0050	151	2
29	0.0238	0.0002	0.2186	0.0079	0.0665	0.0022	146	2
30	0.0232	0.0002	0.1705	0.0083	0.0533	0.0024	146	2
31	0.0235	0.0002	0.1806	0.0089	0.0557	0.0026	148	2
32	0.0237	0.0003	0.1899	0.0106	0.0581	0.0031	148	2

5.2. Geochemistry of wolframite

Wolframite occurs in the G1 of the Shimengsi and Kunshan mining areas, as well as the G2 of the Dawutang and Shiweidong mining areas. It is black to brownish-black in color with euhedral to subhedral crystals ranging from 60 to 150 μm in size, exhibiting tabular, acicular, or hair-like morphologies. Electron microprobe analysis data are presented in Table 3.

The results show that wolframites are primarily composed of WO_3, MnO, and FeO, with trace amounts of Ta_2O_5, MoO_3, and PbO. Significant differences exist in the major element compositions of wolframites from different granites (Figure 7): G1 wolframites range from 74.41% to 77.06% (avg. 76.08%) WO_3, 14.19% -18.85% (avg. 17.29%) FeO, and 5.65%-10.31% (avg. 7.10%) MnO; those of G2 show 75.12% -76.63% (avg. 75.84%) WO_3, 17.52%-21.09% (avg. 19.69%) FeO, and 3.36%- 6.68% (avg. 4.72%) MnO.

The crystal chemical formula of wolframite is determined to be $(Fe_{0.60\text{-}0.89}, Mn_{0.14\text{-}0.44})_{1.01\text{-}1.05}W_{0.98\text{-}1.01}O_4$, indicating a slight deficit in W^{6+} and an excess of Fe^{2+} and Mn^{2+}, with Mn^{2+} being significantly lower in content compared to Fe^{2+}, suggesting that the wolframite is iron-rich. The deficit in W^{6+} may be due to the substitution of W by trace elements, such as Ta and Mo, in the wolframite lattice. WO_3 exhibits a negative correlation with FeO and a positive correlation with MnO in wolframite. A strong linear negative correlation is observed between MnO and FeO (Figure 7). G1 Wolframites contain relatively higher concentrations of WO_3 and MnO, whereas G2 wolframites show significantly higher FeO content.

In addition to major elements such as W, Fe, and Mn in wolframite, the chemical characteristics of trace elements like Ta, Nb, and Mo warrant attention. Wolframites exhibit remarkably high Ta contents (Ta_2O_5: 0.38%-0.64%, avg. 0.50%), whereas Nb contents are extremely low (Nb_2O_5: 0-0.17%, avg. 0.036%). This is a phenomenon relatively uncommon in wolframite. In typical wolframite, Nb content is generally higher than Ta content because Nb exhibits geochemical properties more similar

 doi:10.20944/preprints202510.0931.v1

to W than Ta does, and Nb^{5+} is more likely to substitute for W^{6+} than Ta^{5+}; second, the upper limits of Ta isomorphism in wolframite are Ta_2O_5 (0.3%-0.4%) [20]. Notably, the Ta content in Dahutang granite-related wolframite significantly exceeds this threshold and Nb content. Additionally, no correlation was observed between Nb/Ta contents in wolframite and rock type or with major elements (W, Fe, Mn). As proposed by Zhang, C.Z. et al. [21], the Nb and Ta abundances in wolframite are primarily controlled by the concentrations of these ions in the ore-forming fluid during wolframite crystallization. Thus, the Nb-Ta chemical characteristics of wolframite directly reflect the fluid-melt interactions of Mesozoic peraluminous granites.

The Mo of the wolframite in the Dahutang ore cluster has relatively high content (0.01%-0.25%, avg. 0.152%MoO_3) and substitutes for W^{6+} in the crystal lattice as the hexavalent state.

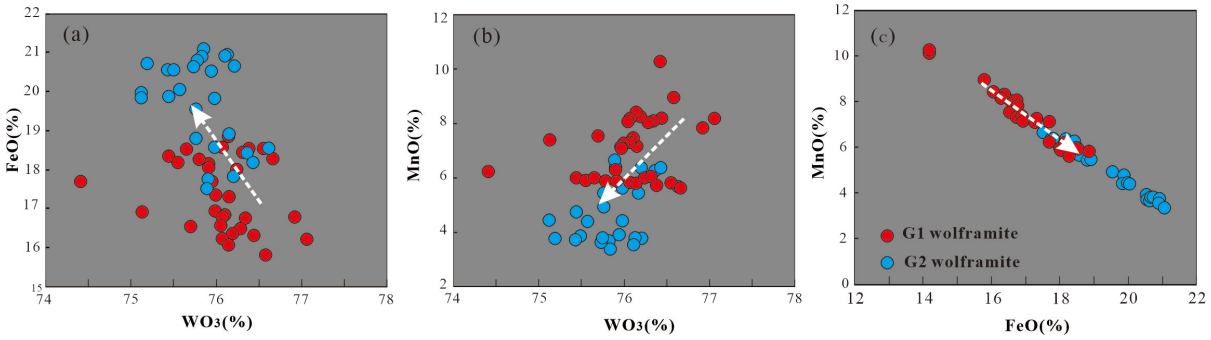

Figure 7. Correlation Diagrams of Oxide Content in Wolframites.

Table 3. Analysis results of electron probe microanalysis for wolframite（%）.

	sample	WO_3	FeO	MnO	CaO	MgO	Ta_2O_5	Nb_2O_5	MoO_3	PbO	Total	Crystal chemical formula
Shimengsi mining area G1 （~150 Ma）	SM-34@1-1	76.44	16.32	8.22	0.03	0.09	0.47	0	0.14	0.11	101.83	(Fe0.69,Mn0.35)1.04W1.01O4
	SM-34@1-3	76.42	14.19	10.31	0.03	0.01	0.61	0	0.09	0.17	101.84	(Fe0.60,Mn0.44)1.04W1.01O4
	SM-34@1-4	74.41	17.70	6.26	0.03	0.14	0.54	0.05	0.15	0.13	99.42	(Fe0.75,Mn0.27)1.02W0.98O4
	SM-34@1-6	76.58	15.80	8.98	0.03	0.03	0.38	0.02	0.06	0.15	102.04	(Fe0.67,Mn0.38)1.05W1.01O4
	SM-34@1-7	77.06	16.22	8.20	0.03	0.07	0.55	0	0.17	0.04	102.35	(Fe0.69,Mn0.35)1.04W1.01O4
	SM-34@1-8	76.15	17.30	7.17	0.03	0.14	0.51	0	0.23	0.18	101.70	(Fe0.73,Mn0.31)1.04W1.00O4
	SM-34@1-9	76.19	16.37	8.27	0.04	0.08	0.50	0.07	0.19	0.12	101.82	(Fe0.69,Mn0.35)1.04W1.01O4
	SM-34@1-10	76.14	16.07	8.45	0.03	0	0.51	0.05	0.19	0.07	101.51	(Fe0.68,Mn0.36)1.04W1.00O4
	SM-34@1-11	75.99	17.33	7.29	0.02	0.06	0.64	0.08	0.16	0.13	101.69	(Fe0.73,Mn0.31)1.04W1.00O4
	SM-34@1-12	76.05	16.56	8.06	0.02	0.16	0.50	0.02	0.03	0.12	101.53	(Fe0.70,Mn0.34)1.04W1.00O4
	SM-34@1-13	76.34	16.75	8.10	0.02	0	0.54	0.05	0.08	0.24	102.12	(Fe0.71,Mn0.35)1.05W1.01O4
	SM-34@1-14	76.07	16.23	8.20	0.03	0	0.54	0.03	0.11	0.14	101.38	(Fe0.69,Mn0.35)1.04W1.00O4

 doi:10.20944/preprints202510.0931.v1

	SM-34@1-15	75.13	16.92	7.41	0.07	0.11	0.52	0.02	0.30	0.10	100.56	(Fe0.72,Mn0.32)1.04 W0.99O4
	SM-34@1-16	76.28	16.50	8.04	0.03	0.05	0.50	0.05	0.22	0.10	101.76	(Fe0.70,Mn0.34)1.04 W1.01O4
	SM-34@1-17	76.92	16.78	7.85	0.01	0.07	0.55	0.04	0.18	0.11	102.52	(Fe0.71,Mn0.34)1.05 W1.01O4
	SM-34@1-18	76.55	18.54	5.83	0.08	0.04	0.51	0	0.01	0.14	101.71	(Fe0.78,Mn0.25)1.03 W1.01O4
	SM-34@1-19	75.95	17.70	7.14	0.03	0.10	0.43	0	0.19	0.21	101.74	(Fe0.75,Mn0.30)1.05 W1.00O4
	SM-34@1-20	76.10	16.83	7.51	0.03	0.09	0.44	0.06	0.12	0.19	101.36	(Fe0.71,Mn0.32)1.03 W1.00O4
	14YSD-3-1@0-1	76.66	18.28	5.65	0.01	0.23	0.51	0	0.20	0.20	101.75	(Fe0.77,Mn0.24)1.01 W1.01O4
	14YSD-3-1@0-2	75.91	18.06	5.92	0.04	0.24	0.42	0	0.15	0.14	100.87	(Fe0.76,Mn0.25)1.01 W1.00O4
	14YSD-3-1@0-3	76.06	16.74	7.35	0.03	0.22	0.37	0.03	0.14	0.15	101.09	(Fe0.71,Mn0.31)1.02 W1.00O4
	14YSD-3-1@0-4	75.91	18.16	6.31	0.01	0.170	0.40	0.01	0.18	0.28	101.43	(Fe0.77,Mn0.27)1.04 W1.00O4
	14YSD-3-1@0-5	75.98	16.94	7.11	0.02	0.28	0.42	0.04	0.25	0.16	101.22	(Fe0.72,Mn0.30)1.02 W1.00O4
	14YSD-3-1@1-1	75.65	18.53	6.02	0.06	0.20	0.51	0.08	0.11	0.16	101.40	(Fe0.78,Mn0.26)1.04 W1.00O4
Kunshan mining area G1 （~150 Ma）	14YSD-5-1@1-2	76.24	18.01	6.02	0.04	0.14	0.50	0.02	0.14	0.23	101.34	(Fe0.76,Mn0.26)1.02 W1.00O4
	14YSD-3-1@1-3	75.44	18.34	6.03	0.04	0.24	0.46	0.03	0.22	0.12	100.92	(Fe0.78,Mn0.26)1.04 W0.99O4
	14YSD-3-1@1-4	75.80	18.27	5.88	0.10	0.20	0.43	0	0.19	0.12	100.99	(Fe0.77,Mn0.25)1.02 W1.00O4
	14YSD-3-1@1-5	76.31	18.45	6.07	0.01	0.20	0.51	0	0.14	0.09	101.78	(Fe0.78,Mn0.26)1.04 W1.01O4
	14YSD-3-1@1-6	76.38	18.55	5.73	0.04	0.19	0.55	0.14	0.08	0.09	101.74	(Fe0.78,Mn0.24)1.02 W1.01O4
	14YSD-3-1@3-5	76.07	18.57	5.86	0.02	0.17	0.43	0.01	0.14	0.18	101.46	(Fe0.78,Mn0.25)1.03 W1.00O4
	14YSD-3-1@3-6	75.70	16.54	7.55	0.03	0.29	0.44	0.06	0.16	0.17	100.92	(Fe0.70,Mn0.32)1.02 W0.99O4
	14YSD-3-1@3-7	75.55	18.19	5.93	0.04	0.21	0.50	0.04	0.138	0.14	100.74	(Fe0.77,Mn0.25)1.04 W0.99O4
	14YSD-3-1@3-8	76.14	18.85	5.81	0.02	0.15	0.57	0	0.23	0.12	101.88	(Fe0.80,Mn0.25)1.05 W1.00O4
	14SWD-10@1-1	76.10	20.91	3.59	0.02	0.17	0.49	0.02	0.20	0.18	101.68	(Fe0.88,Mn0.15)1.03 W1.00O4
Shiweidong mining area G2（～140 Ma）	14SWD-10@1-2	75.98	18.58	5.66	0	0.24	0.47	0	0.21	0.16	101.28	(Fe0.79,Mn0.24)1.03 W1.00O4
	14SWD-10@1-3	76.63	18.55	5.67	0.04	0.20	0.48	0.01	0.01	0.18	101.77	(Fe0.78,Mn0.24)1.02 W1.01O4
	14SWD-10@1-5	76.36	18.43	6.28	0.01	0.17	0.56	0	0.06	0.16	102.03	(Fe0.78,Mn0.27)1.04 W1.01O4
	14SWD-10@1-6	76.20	17.83	6.40	0.04	0.23	0.64	0	0.17	0.24	101.74	(Fe0.75,Mn0.27)1.02 W1.00O4

 doi:10.20944/preprints202510.0931.v1

	14SWD-10@1-7	75.76	18.81	5.45	0	0.12	0.48	0	0.27	0.15	101.03	(Fe0.80,Mn0.23)1.03W1.00O4
	14SWD-10@1-8	75.90	17.75	6.41	0.02	0.26	0.52	0.02	0.22	0.17	101.27	(Fe0.75,Mn0.27)1.02W1.00O4
	14SWD-10@2-1	75.49	20.54	3.88	0.02	0.16	0.53	0.05	0.16	0.10	100.92	(Fe0.87,Mn0.17)1.04W0.99O4
	14SWD-10@2-2	75.43	20.55	3.73	0.02	0.20	0.49	0	0.17	0.22	100.81	(Fe0.87,Mn0.16)1.03W0.99O4
	14SWD-10@2-3	76.21	20.66	3.81	0.01	0.19	0.47	0.07	0.22	0.12	101.76	(Fe0.87,Mn0.16)1.03W1.00O4
	14SWD-10@2-4	75.85	21.09	3.36	0.01	0.13	0.52	0.02	0.18	0.11	101.27	(Fe0.89,Mn0.14)1.03W1.00O4
	14SWD-10@2-5	75.76	19.55	4.96	0.03	0.05	0.51	0.05	0.11	0.25	101.26	(Fe0.83,Mn0.21)1.04W1.00O4
	14SWD-10@3-1	76.13	20.93	3.78	0	0.24	0.48	0.04	0.09	0.14	101.82	(Fe0.88,Mn0.16)1.04W1.01O4
	14SWD-10@3-2	75.73	20.65	3.67	0.01	0.14	0.51	0.03	0.17	0.20	101.11	(Fe0.87,Mn0.16)1.03W1.00O4
	14SWD-10@3-3	75.75	20.76	3.80	0.02	0.17	0.51	0	0.16	0.18	101.34	(Fe0.88,Mn0.16)1.04W1.00O4
	14SWD-10@3-4	75.83	20.90	3.65	0.02	0.18	0.56	0	0.12	0.21	101.46	(Fe0.88,Mn0.16)1.04W1.00O4
	14SWD-10@3-5	75.94	20.53	3.93	0.02	0.20	0.48	0	0.16	0.17	101.43	(Fe0.87,Mn0.17)1.04W1.00O4
	14YKD-1@1-1	75.44	19.87	4.76	0.05	0.01	0.48	0.09	0.11	0.21	101.03	(Fe0.84,Mn0.20)1.04W1.00O4
	14YKD-1@1-2	75.57	20.05	4.42	0.03	0	0.60	0.08	0.09	0.10	100.95	(Fe0.85,Mn0.19)1.04W1.00O4
	14YKD-1@1-3	75.19	20.72	3.80	0	0.01	0.49	0.12	0.10	0.08	100.51	(Fe0.88,Mn0.16)1.04W0.99O4
Dawutang mining area G2（～140 Ma）	14YKD-1@1-4	75.89	17.52	6.68	0.05	0.02	0.47	0.01	0.10	0.14	100.89	(Fe0.74,Mn0.29)1.03W1.00O4
	14YKD-1@1-5	76.43	18.18	6.39	0.03	0.02	0.63	0.10	0.09	0.18	102.04	(Fe0.77,Mn0.27)1.04W1.01O4
	14YKD-1@1-6	75.12	19.85	4.46	0.08	0.08	0.45	0.09	0.17	0.11	100.45	(Fe0.84,Mn0.19)1.03W0.99O4
	14YKD-1@1-7	75.98	19.82	4.43	0.07	0.06	0.51	0.05	0.10	0.06	101.07	(Fe0.84,Mn0.19)1.03W1.00O4
	14YKD-1@1-8	75.12	19.98	4.48	0.16	0.01	0.46	0.17	0.23	0.08	100.70	(Fe0.84,Mn0.19)1.03W0.99O4
	14YKD-1@1-10	76.15	18.91	5.48	0.05	0.07	0.44	0.13	0.21	0.02	101.45	(Fe0.80,Mn0.23)1.03W1.00O4

5.3. Whole-rock chemistry of Mesozoic granites

Total 22 whole-rock elemental compositions of the Mesozoic granites are analyzed in this study (Table 4), including 14 G1 granites from the Shimensi mining area and the Kunshan mining area; 8 G2 granites from the Dawutang mining area. 20 previously reported bulk-rock geochemistry are also included for the following discussions (Table 4). Among them 3 G2 granites from the Shiweidong mining area [22]; 11 G3 granites from the Dawutang mining area [23]; 6 G4 granites from the Dawutang mining area [24].

Overall, the Mesozoic granites are characterized by high and variable SiO_2 (70.7%-75.52%), Al_2O_3 (12.92%-16.58 %), low MgO (0.03%-0.54%) and CaO (0.30%-1.34%) (Table 5). G1 granites have the lowest average MgO and higher abundances of TiO2, TFeO and CaO relative to the G2-G4 granites

 doi:10.20944/preprints202510.0931.v1

(Figure 8a, 8c, 8d and 8g). In the SiO_2 vs. alkali (Na_2O+K_2O) diagrams (Figure 9a and 9b), most data points plot within the calc-alkaline granite field, but G2-G4 granites have relative highly fractionated trend. All granites are strongly peraluminous, with aluminum saturation indicates ACNK ranging from 1.10 to 1.67, falling within the peraluminous field in the A/NK vs. A/CNK diagram (Figure 9c). On the harker diagrams, major elements Al_2O_3, MnO, P_2O_5 and K_2O show differing behaviour across the G1 and G2-G4 granites (Figure 8b, 8e, 8f and 8h). In the G1 granite, the contents of Al_2O_3, MnO, and P_2O_5 remain basically unchanged and do not vary with the MgO content, while the K_2O content is negatively related to MgO. However, in the G2-G4 granites, the contents of Al_2O_3, MnO, and P_2O_5 are negatively related to MgO, whereas the K_2O content is positively related to MgO.

The K/Al versus Na/Al molar ratio diagram (Figure 9d) was used to characterize at the alteration trends of the Mesozoic peraluminous granites. The logic behind this method is that minimally altered igneous rock samples typically exhibit relatively balanced major element compositions. In contrast, metasomatized rocks display distinct chemical signatures, characterized by the dominance of one or two major elements (e.g., Na, K), which reflect the nature of hydrothermal alteration processes such as albitization, K-feldspathization, muscovitization, or greisenization. Most of the data points plot approximately at the middle region of unaltered granite with Na/Al molar ratios 0.3-0.5 [29]. The G1 granite exhibits a little greisenization trend which is characterized by low (<0.3) Na/Al molar ratio values for variable K/Al molar ratios (0.1-0.4). The G2-G4 granites show pronounced albitization accompanied by increase in the Na/Al molar ratio (>0.5) and decrease in the K/Al molar ratio (<0.3), exemplified by the G4 granite which is the product of the albitization of G2/G3 granite. The alteration trends revealed by the major element composition of the granite are consistent with the field petrographic observations.

The Mesozoic granites exhibit right-leaning profiles with enrichment in light rare earth elements (LREE), characterized by LREE/HREE fractionation and negative Eu anomalies (Figure 10). G4 is distinguished by severely Eu-depleted (Eu < 0.05 ppm), and pronounced M-type REE tetrad effects ($TE_{1,3}$ values up to 1.28; [19]). Ba, Sr, Th, U, Zr and the REE are lower and Rb higher in the geochemically evolved G2-G4 granites, which also have stronger Eu anomalies, relative to the G1 granites, sharing the features of those S-type granites. The extremely low Sr and Ba concentrations likely result from intensive fractionation of plagioclase and K-feldspar, which incorporate these elements into their lattices and deplete them from the residual melt. Conversely, Rb—being incompatible in feldspars—accumulates preferentially in the residual melt during fractionation, leading to the high Rb content typical of highly fractionated granites. Notably, Ta and Nb display significant fractionation, with high Ta and low Nb.

 doi:10.20944/preprints202510.0931.v1

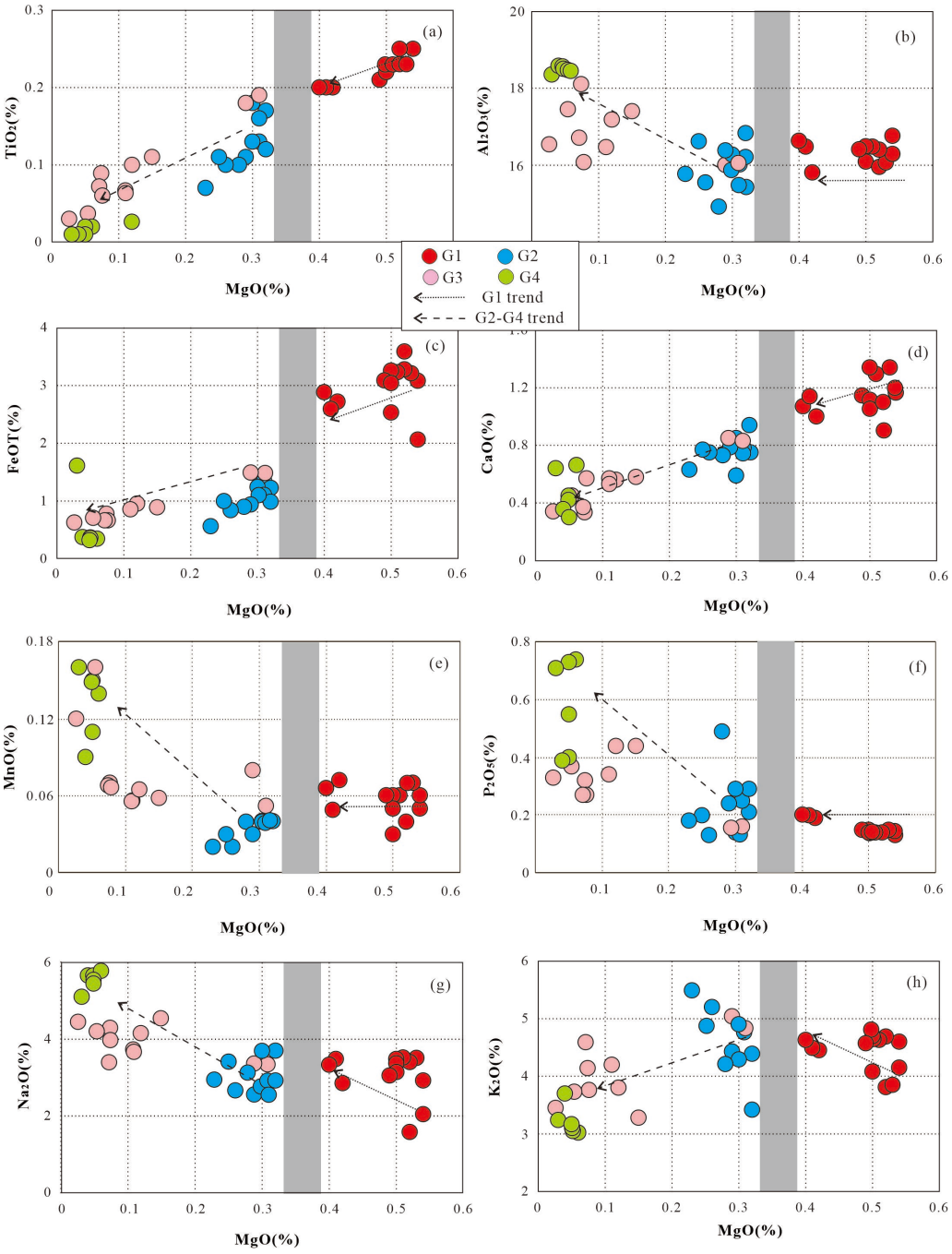

Figure 8. Harker diagrams of major elements of Mesozoic granites in the Dahutang orefield.

 doi:10.20944/preprints202510.0931.v1

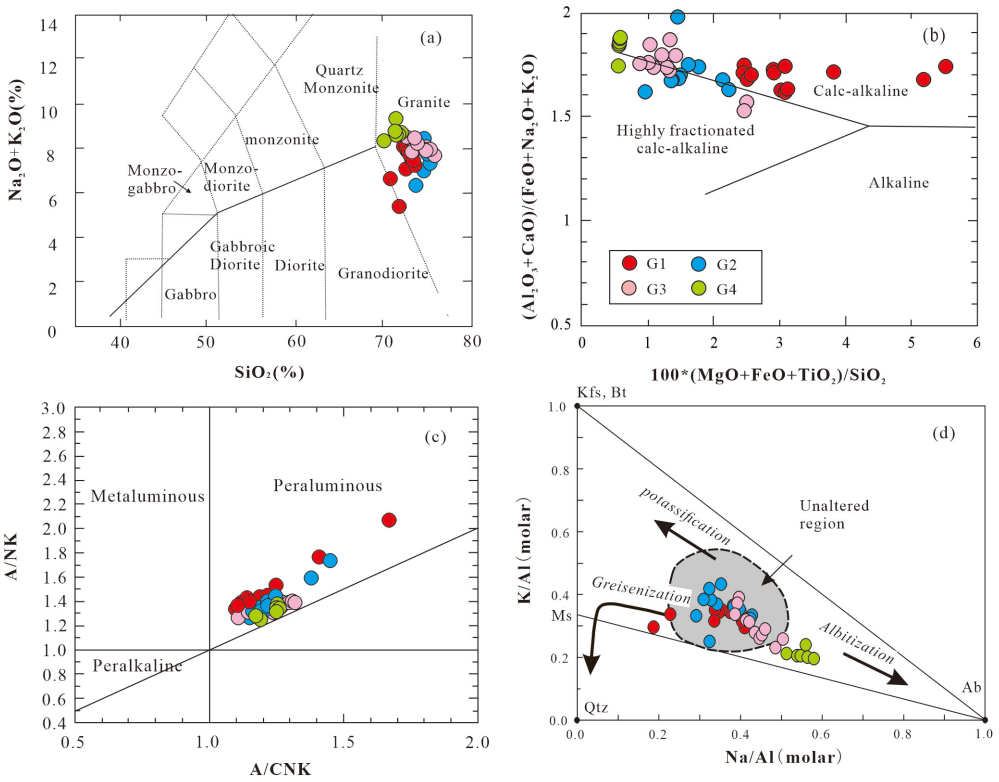

Figure 9. (a) SiO_2 vs. (K_2O + Na_2O) diagram [25]; (b) 100*(MgO+FeO+TiO_2)/SiO_2 vs. (Al_2O_3+CaO)/(FeO+NaO+K_2O) diagram [26] for rocks with >68 wt.% SiO_2, (c) Molar Al_2O_3/(Na_2O + K_2O) versus Al_2O_3/(CaO + Na_2O + K_2O) [27], and (d) K/Al versus Na/Al molar ratio diagram [28]. Ab = albite, Bt = biotite, Kfs = Kfeldspar, Ms = muscovite, Qtz = quartz. The compositional field for the least-altered peraluminous granites from the French Massif Central is shown for reference (dashed line).

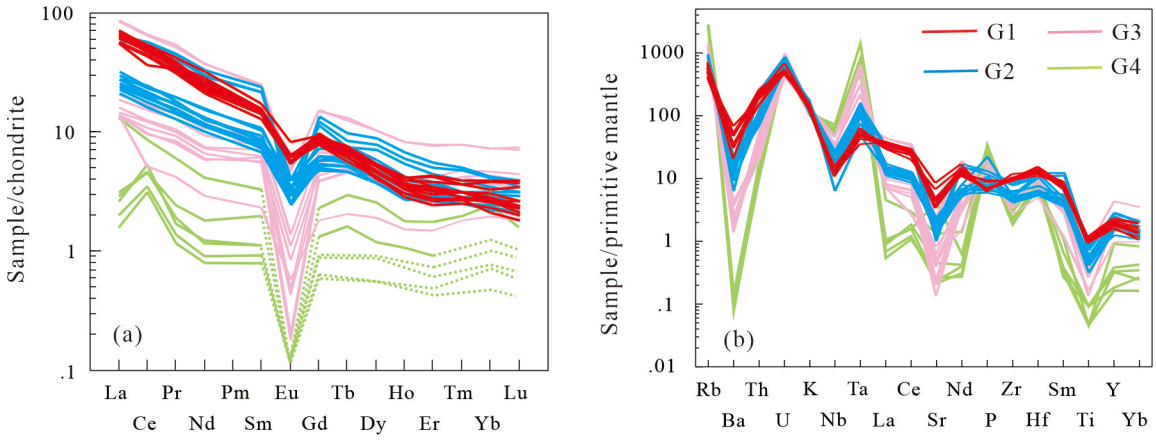

Figure 10. Chondrite-normalized REE distribution patterns and trace element spider diagrams of granites in the Dahutang orefield. Normalization values from [30]. The dashed lines of albite granites represent the inferred trend.

Table 4. Analysis data of major elements (wt.%) and trace elements （ppm） from Mesozoic granite in the Dahutang District.

Deposit	Shimengsi mining area	Kunshan mining area	Dawutan mining area
Rock	Biotite granite (G1，~150 Ma)		Two-mica granite（G2，~140 Ma）

 doi:10.20944/preprints202510.0931.v1

Sample	SM-4	SM-6	SM-18	SM-19	SM-20	SM-29	SM-48	SM-50	SM-51	SM-52	SM-53	12YSD-22	12YSD-23	12YSD-24	1281-1	1281-5	1281-6	1281-9
SiO_2	72.54	72.33	72.44	72.86	73.73	72.85	72.32	72.72	72.46	73.13	73.33	71.71	70.75	72.52	74.7	73.6	75.17	75.35
TiO_2	0.23	0.22	0.2	0.2	0.2	0.21	0.22	0.23	0.23	0.23	0.22	0.25	0.25	0.25	0.1	0.12	0.13	0.1
Al_2O_3	14.4	14.44	14.63	14.48	13.81	14.41	14.47	14.49	14.48	14.07	14.09	13.95	14.76	14.29	12.92	14.83	13.48	13.55
Fe_2O_3	2.04	1.94	1.79	1.58	1.7	1.83	1.6	1.81	1.88	1.91	1.81	0.45	0.21	0.08	0.2	0.07	0.25	0.2
FeO	1.44	1.51	1.27	1.17	1.19	1.44	1.09	1.38	1.52	1.49	1.41	3.18	2.89	1.99	0.72	0.93	0.88	0.66
MnO	0.079	0.082	0.066	0.049	0.072	0.06	0.03	0.05	0.06	0.07	0.06	0.04	0.05	0.06	0.04	0.04	0.04	0.02
MgO	0.52	0.5	0.4	0.41	0.42	0.49	0.5	0.5	0.51	0.53	0.5	0.52	0.54	0.54	0.28	0.32	0.31	0.26
CaO	1.1	1.11	1.07	1.14	1	1.15	1.04	1.1	1.29	1.34	1.34	0.9	1.17	1.19	0.73	0.94	0.79	0.75
Na_2O	3.4	3.37	3.33	3.48	2.85	3.05	3.36	3.11	3.52	3.51	3.46	1.58	2.04	2.92	3.13	2.92	2.55	2.66
K_2O	4.69	4.75	4.63	4.49	4.45	4.57	4.81	4.65	4.63	3.85	4.08	3.81	4.6	4.15	4.21	3.42	4.77	5.2
P_2O_5	0.15	0.15	0.2	0.2	0.19	0.15	0.15	0.15	0.14	0.15	0.14	0.14	0.13	0.14	0.49	0.21	0.14	0.13
LOI	0.86	1.07	1.15	1.01	1.35	1.18	1.28	1.15	0.73	1.21	0.97	2.35	1.78	1.49	1.14	1.72	1.02	0.82
Total	101.45	101.47	101.18	101.07	100.96	101.39	100.87	101.34	101.45	101.49	101.41	98.88	99.17	99.62	98.66	99.12	99.53	99.7
A/CNK	1.14	1.14	1.17	1.14	1.22	1.19	1.14	1.19	1.10	1.14	1.12	1.67	1.41	1.25	1.17	1.45	1.25	1.19
W	4.45	4.17	33.5	9.84	86.8	46.1	12.4	18.4	27.2	28.2	11.8	34.33	62.40	8.01	15.5	1026	13.8	31.50
Ba	328	331	217	213	227	326	336	353	352	142	211	243	471	216	129	120	149	116
Rb	318	355	410	364	440	384	352	347	304	320	293	314	258	253	562	469	389	393
Sr	98.4	90.2	72.9	70	72.1	90.1	87.9	92.1	100	91.2	93.7	77.4	177	138	48.7	36.3	47.1	35.3
Y	8.55	8.07	7.52	7.02	8.48	8.69	9.16	8.81	8.25	9.14	8.81	9.92	9.46	10.5	10.5	8.08	8.54	9.17
Zr	111	100	104	101	104	105	109	105	108	103	109	105	129	114	57.3	50.2	67.5	55.6
Nb	9.22	8.15	8.92	8.6	8.54	7.99	7.49	7.81	7.72	7.77	7.94	10.5	8.68	10.8	16.4	11.1	12.5	10.6
Th	19.4	16.4	15.9	16.1	17	17.7	20.9	18	19.6	18.9	18.4	12.4	15.1	12	8.15	7.18	7.92	6.55
Hf	4.2	4.1	3.7	3.8	4.6	4.6	4.6	4.3	3.9	4.4	4	3.37	3.78	3.58	1.95	1.75	2.38	2.03
Ta	2.35	2.33	2.52	2.54	2.13	2	1.98	1.9	1.7	1.88	1.98	2.01	1.42	2.08	6.71	3.88	4.37	4.84
U	10.4	9.35	11.3	10.6	10	14.3	11.2	9.37	9.72	10.5	10.2	10.7	9.41	10.3	14	15.9	11.6	14.1
Li	131	183	197	173	250	177	158	150	155	186	134	54.6	51.8	51.5	1243	500	221	145
Mo	0.98	0.9	1.62	1.07	1.17	8.52	0.24	1.33	1	0.62	1	2.97	0.15	0.67	1.01	0.55	5.71	7.19
Sn	8.71	19.5	34.7	26	55.6	36	24.1	20.3	12.1	28.3	14.2	24.2	17.6	8.55	310	138	52.6	38.2
Cu	6.69	58.1	104	28.4	555	350	146	338	10.3	80.2	16.5	1443	551	240	345	53.7	310	150
La	24.3	20.9	20.4	20.5	23.1	23.2	25.7	25.9	24.6	22.6	23.6	22.1	25.3	20.3	10.8	9.35	10.2	8.37
Ce	50.3	41.5	41	41.7	47.4	44.4	49.6	50.7	49	44.9	46	45.4	51.5	35	22.1	19.2	19.7	16.8
Pr	5.31	4.29	4.43	4.53	5.04	4.78	5.25	5.33	5.19	4.73	4.84	4.96	5.71	4.64	2.65	2.02	2.34	1.96
Nd	18.4	14.9	15.6	15.7	17.4	16.3	18.2	17.5	17.4	15.8	16.4	20.1	22.6	18.9	10.8	8.22	9.19	7.77
Sm	3.56	2.99	3.27	3.26	3.64	3.24	3.62	3.52	3.45	3.31	3.33	3.58	3.97	3.42	2.48	1.66	1.98	1.72
Eu	0.55	0.49	0.47	0.49	0.49	0.53	0.55	0.55	0.53	0.49	0.47	0.56	0.72	0.55	0.3	0.27	0.34	0.26
Gd	2.84	2.4	2.56	2.51	2.72	2.58	2.93	2.82	2.86	2.46	2.97	2.75	2.82	2.69	2.43	1.46	1.92	1.77
Tb	0.4	0.33	0.36	0.36	0.38	0.35	0.41	0.39	0.38	0.35	0.4	0.44	0.43	0.43	0.44	0.27	0.34	0.34
Dy	1.79	1.61	1.52	1.6	1.81	1.75	1.95	1.99	1.95	1.71	2.06	2.06	2.04	2.04	2.22	1.42	1.8	1.83
Ho	0.29	0.26	0.26	0.24	0.28	0.3	0.31	0.32	0.32	0.29	0.36	0.35	0.33	0.35	0.36	0.25	0.29	0.31
Er	0.79	0.66	0.69	0.61	0.69	0.8	0.85	0.78	0.82	0.74	0.86	1.05	0.96	1.07	0.94	0.72	0.81	0.86
Tm	0.1	0.097	0.095	0.09	0.099	0.1	0.11	0.11	0.11	0.11	0.11	0.13	0.13	0.14	0.11	0.1	0.1	0.11
Yb	0.65	0.65	0.52	0.57	0.64	0.65	0.67	0.7	0.68	0.64	0.76	0.94	0.82	0.98	0.7	0.69	0.69	0.73
Lu	0.09	0.08	0.07	0.077	0.086	0.1	0.09	0.09	0.09	0.09	0.1	0.14	0.13	0.15	0.1	0.1	0.1	0.11
Eu/Eu*	0.51	0.54	0.48	0.5	0.46	0.54	0.5	0.52	0.5	0.5	0.45	0.53	0.63	0.54	0.37	0.52	0.53	0.45
$(La/Yb)_N$	26.82	23.06	28.14	25.8	25.89	25.6	27.51	26.54	25.95	25.33	22.27	16.86	22.13	14.86	11.07	9.72	10.6	8.22

 doi:10.20944/preprints202510.0931.v1

ΣREE	109.37	91.16	91.24	92.24	103.78	99.08	110.24	110.7	107.38	98.22	102.26	104.56	117.46	90.66	56.43	45.73	49.8	42.94
T_{Zr}(℃)	762	754	760	756	766	763	762	763	757	757	761	790	795	775	717	721	735	716
Deposit	**Dawutan mining area**						**Shiweidong mining area(Cited from [23])**				**Dawutang mining area (Cited from [24])**							
Rock	**Two-mica granite（G2，~140 Ma）**										**Muscovite granite（G3,~140 Ma）**							
Sample	1281-10	1281-11	1281-12	1281-21	Zk0-26-1	Zk0-26-2	Zk0-26-3	白1	白2	白3	白4	白5	白6	白7				
SiO_2	74.54	73.96	74.53	74.75	72.52	72.88	73.33	73.5	75.52	74.61	72.67	74.54	75.1	74.6				
TiO_2	0.13	0.11	0.11	0.07	0.17	0.18	0.16	0.037	0.059	0.072	0.089	0.065	0.03	0.062				
Al_2O_3	13.91	14.62	14.38	13.77	14.21	14.27	14.02	15.45	14.08	14.71	16.1	14.46	14.54	14.46				
Fe_2O_3	0.36	0.3	0.29	0.15	0.14	0.12	0.28	0.043	0.052	0.011	0.076	0.032	0.03	0.063				
FeO	0.77	0.74	0.68	0.43	1.1	1.12	1.1	0.67	0.62	0.68	0.71	0.82	0.6	0.8				
MnO	0.04	0.03	0.03	0.02	0.04	0.04	0.04	0.16	0.07	0.068	0.066	0.056	0.12	0.056				
MgO	0.3	0.25	0.29	0.23	0.32	0.3	0.31	0.054	0.076	0.071	0.074	0.11	0.026	0.11				
CaO	0.85	0.77	0.79	0.63	0.75	0.59	0.73	0.44	0.57	0.37	0.34	0.53	0.34	0.57				
Na_2O	2.77	3.41	2.56	2.95	3.7	3.69	2.92	4.21	3.94	3.42	4.3	3.71	4.46	3.66				
K_2O	4.9	4.88	4.43	5.49	4.39	4.27	4.77	3.73	3.76	4.59	4.14	4.2	3.45	4.2				
P_2O_5	0.14	0.2	0.24	0.18	0.29	0.29	0.25	0.37	0.27	0.27	0.32	0.34	0.33	0.34				
LOI	0.95	0.77	1.2	0.94	1.5	1.56	1.59	1.26	0.96	1.04	1.04	1.04	0.88	0.97				
Total	99.66	100.04	99.53	99.61	99.13	99.31	99.5	99.92	99.98	99.91	99.93	99.9	99.91	99.89				
A/CNK	1.22	1.19	1.38	1.15	1.16	1.21	1.24	1.31	1.21	1.30	1.32	1.24	1.24	1.24				
W	43.60	8.57	21.80	12.70	33.1	27.9	101	30.7	334	548	84.1	80.4	106	73.1				
Ba	155	109	148	137	79.6	45.2	135	18.4	11.3	13.7	10	31.5	10	25.8				
Rb	445	397	400	346	616	571	707	922	482	562	844	458	782	468				
Sr	50.7	32.2	39.3	41.5	24.9	21.7	36.7	12.1	4.38	5.36	2.94	10.7	17.6	8.95				
Y	10.1	7.95	8.06	6.99	12.6	13.3	11.5	4.64	9.14	11.8	10.3	7.66	9.75	7.2				
Zr	71	49.7	51.7	58.2	91.1	98.3	88.5	31.2	46.4	60	48.4	41.2	52.6	41.5				
Nb	12.4	14.1	13.7	4.55	18.5	19.6	16.6	33.3	25	26.3	34.3	17.2	34.6	17.9				
Th	8.6	6.8	8.1	7.33	19.42	21.1	20.3	1.72	3.18	4.94	3.7	2.27	4.02	2.24				
Hf	2.37	1.78	1.93	1.97	3.44	3.84	3.25	1.57	2.14	2.1	2.14	2.38	2.64	2.19				
Ta	4.28	6.29	6.04	1.99	5.58	6.11	4.53	27.4	13.6	9.01	13.6	4.18	23.4	4.62				
U	13.1	13.7	14.4	11.5	17.6	18.11	15.9	11.7	17.8	21.4	20	9.04	16.4	10.7				
Li	209	159	272	132	269	301	232	1050	272	334	455	262	225	321				
Mo	0.72	0.62	1.89	2.45	1.22	1.86	0.97	1.52	12.2	2.01	0.59	0.61	0.88	7.52				
Sn	50.1	41.1	96	27.6	81.6	52.7	65.8	251	75.0	80.0	65.8	37.5	108	61.1				
Cu	68.3	109	344	46.7	103	6.07	395	31.8	92.6	41.3	41.4	23.9	228	32.7				
La	11.8	8.83	10.1	9.02	21.3	23.3	22.5	5	5	6.88	5.38	5.8	5	5				
Ce	22.8	18	20.5	18.2	50.4	54	53.4	4.92	10.4	14.6	11.8	12	9.06	9.3				
Pr	2.69	2.08	2.29	2.13	5.61	6.26	5.89	0.57	1.26	1.74	1.38	1.43	1.14	1.09				
Nd	11	8.25	9.2	8.31	20.6	23.5	20.9	2.07	4.72	6.61	5.15	5.34	4.18	4.15				
Sm	2.36	1.76	1.94	1.85	4.94	5.46	5	0.54	1.29	1.78	1.44	1.63	1.3	1.4				
Eu	0.34	0.21	0.29	0.25	0.28	0.21	0.35	0.051	0.038	0.042	0.018	0.096	0.016	0.073				
Gd	2.23	1.61	1.76	1.64	3.72	4.15	3.46	0.55	1.18	1.67	1.32	1.6	1.2	1.42				
Tb	0.4	0.3	0.33	0.3	0.49	0.57	0.43	0.12	0.26	0.35	0.29	0.32	0.27	0.28				
Dy	2.07	1.58	1.69	1.4	2.94	3.36	2.71	0.72	1.52	2.02	1.68	1.64	1.78	1.5				
Ho	0.33	0.26	0.28	0.23	0.51	0.57	0.46	0.13	0.27	0.35	0.31	0.25	0.28	0.24				
Er	0.91	0.72	0.77	0.67	1.26	1.39	1.1	0.37	0.82	1.04	0.92	0.64	0.88	0.6				
Tm	0.11	0.09	0.1	0.09	0.17	0.18	0.14	0.064	0.15	0.17	0.15	0.091	0.15	0.089				
Yb	0.77	0.61	0.65	0.58	1.01	1.04	0.85	0.49	0.9	1.14	1.06	0.59	1.07	0.56				
Lu	0.12	0.09	0.09	0.08	0.13	0.15	0.12	0.069	0.13	0.17	0.15	0.082	0.15	0.075				
Eu/Eu*	0.45	0.37	0.47	0.43	0.19	0.13	0.24	0.28	0.09	0.07	0.04	0.18	0.04	0.16				
$(La/Yb)_N$	10.99	10.38	11.15	11.16	15.13	16.07	18.99	7.32	3.98	4.33	3.64	7.05	3.35	6.4				
ΣREE	57.93	44.39	49.99	44.75	113.36	124.14	117.31	15.66	27.94	38.56	31.05	31.51	26.48	25.78				
T_{Zr}(℃)	736	705	720	716	750	760	754	678	703	727	709	696	714	696				
Deposit	**Dawutang mining area(Cited from [24])**				**Dawutan mining area (Cited from [19])**													
Rock	**Muscovite granite（G3,~140 Ma）**				**Albite granite（G4, ~140 Ma）**													
Sample	白8	白9	白10	白11	PM-06	PM-07	PM-08	PM-09	PM-10	PM-11								
SiO_2	73.77	73.36	73.36	73.2	71.29	71.37	71.51	71.28	70.03	71.99								
TiO_2	0.19	0.18	0.1	0.11	0.02	0.01	0.02	0.02	0.01	0.01								
Al_2O_3	14.05	14	15.18	15.4	16.41	16.58	16.51	16.52	16.35	16.42								
Fe_2O_3	0.15	0.17	0.15	0.2	0.01	0.02	0.01	0.01	0.17	0.02								
FeO	1.34	1.34	0.82	0.71	0.34	0.35	0.36	0.35	1.46	0.35								
MnO	0.052	0.08	0.066	0.58	0.14	0.09	0.15	0.15	0.16	0.11								

 doi:10.20944/preprints202510.0931.v1

MgO	0.31	0.29	0.12	0.15	0.06	0.04	0.05	0.05	0.03	0.05
CaO	0.83	0.85	0.56	0.58	0.67	0.35	0.44	0.4	0.64	0.3
Na_2O	3.35	3.37	4.16	4.55	5.78	5.64	5.41	5.48	5.09	5.63
K_2O	4.82	5.04	3.8	3.28	3.02	3.7	3.2	3.15	3.24	3.08
P_2O_5	0.16	0.16	0.44	0.44	0.74	0.39	0.55	0.73	0.71	0.4
LOI	0.83	1.01	1.15	1.24	1.01	0.94	1.24	1.19	1.26	1.09
Total	99.85	99.85	99.91	100.44	99.53	99.52	99.49	99.37	99.31	99.49
A/CNK	1.15	1.11	1.27	1.27	1.17	1.19	1.25	1.26	1.25	1.25
W	27.7	20.3	54.6	76.1	644	801	694	481	21.6	576
Ba	216	202	17.7	26.8	1.01	0.9	0.64	0.87	17.2	0.53
Rb	410	452	632	572	1581	1622	1733	1825	1750	1716
Sr	50.8	45.8	8.54	13.2	88.4	4.93	5.54	9.44	27.8	4.49
Y	20.1	20.1	9.77	10.5	1.73	1.49	0.83	1.47	4.14	0.74
Zr	124	120	54.2	53.8	33.7	25.9	41.4	24.4	24.1	20.6
Nb	18.3	17.6	22	24.3	43.6	43.1	41.8	45.4	51.3	38.2
Th	24.6	24.3	2.98	2.68	1.43	1.44	0.84	1.37	2.2	0.97
Hf	3.02	2.88	2.64	2.93	3.02	2.53	3.72	2.76	2.07	2.29
Ta	3.4	3.16	22	9.5	19.3	33.5	22.5	27.9	57.9	21.9
U	11.3	12.2	14.9	14.8	13.8	12	11.9	11.4	14.1	12
Li	280	241	892	873	1434	924	1866	2367	2053	1792
Mo	1.42	1.75	1.08	1.09	-	-	-	-	-	-
Sn	53.4	34.9	92.8	90.6	159	368	67	76.8	369	79.9
Cu	20.9	11.9	11.2	79.9	19.4	98.6	4.65	3.07	9.3	11.1
La	31.3	30.5	7.63	7.54	0.73	0.68	0.37	0.61	3.12	0.47
Ce	63.4	61	16.2	15.9	2.77	2.83	1.91	3.25	5.25	2.13
Pr	7.38	7.04	1.96	1.96	0.23	0.18	0.11	0.16	0.57	0.13
Nd	26.7	26.4	7.57	7.7	0.84	0.54	0.37	0.57	1.92	0.42
Sm	5.7	5.64	2.08	2.04	0.3	0.17	0.12	0.17	0.5	0.14
Eu	0.42	0.4	0.12	0.12	<0.05	<0.05	<0.05	<0.05	<0.05	<0.05
Gd	4.57	4.71	2.04	2.04	0.27	0.18	0.12	0.19	0.47	0.13
Tb	0.76	0.73	0.4	0.37	0.06	<0.05	<0.05	<0.05	0.11	<0.05
Dy	3.9	3.95	2.02	1.9	0.3	0.23	0.14	0.22	0.65	0.14
Ho	0.7	0.7	0.31	0.31	0.06	<0.05	<0.05	<0.05	0.1	<0.05
Er	1.96	1.91	0.82	0.82	0.15	0.12	0.08	0.1	0.29	0.07
Tm	0.28	0.28	0.14	0.11	<0.05	<0.05	<0.05	<0.05	0.05	<0.05
Yb	1.78	1.79	0.76	0.74	0.21	0.17	0.13	0.12	0.41	0.08
Lu	0.28	0.27	0.1	0.11	<0.05	<0.05	<0.05	<0.05	0.04	<0.05
Eu/Eu*	0.24	0.23	0.18	0.18	-	-	-	-	-	-
$(La/Yb)_N$	12.61	12.22	7.2	7.31	2.49	2.87	2.04	3.65	5.53	4.21
ΣREE	149.13	145.32	42.15	41.66	-	-	-	-	-	-
T_{Zr}(℃)	775	769	716	715	673	656	693	656	654	645

5.4. Characteristics of Zr/Hf, Y/Ho, Nb/Ta, and K/Rb isovalent ratios

In pure magmatic fractionation, isovalent element ratios like Y/Ho and Zr/Hf stay coherent and near chondritic levels, as mineral-melt fractionation depends on ionic substitution in lattices (governed by charge and radius)—termed CHARAC behavior [31]. By contrast, fluid-driven leaching or precipitation, influenced by elements' distinct chemical properties, causes non-CHARAC behavior, disrupting coherence between isovalent "twins." Highly evolved, H_2O-Li-P-B-Cl-rich magmas show such unusual non-CHARAC ratios [31, 32].

The Y/Ho ratios in G1–G3 granites range from 23.33 to 35.69, which are close to the chondritic ratio (Y/Ho=28) [33] (Table 5; Figure 11a). In contrast, the Y/Ho ratios in G4 granites (14.8–41.4) deviate slightly from the chondritic ratio, indicating non-CHARAC behavior and a moderately evolved composition. Similarly, the Zr/Hf ratios follow a comparable pattern: in G1, G2, and G3 granites, the Zr/Hf ratios vary between 17.31 and 41.67, whereas in G4 granite, they range from 8.84 to 11.64 (Table 5; Figure 11a). The Zr/Hf ratios in G1–G3 granites are close to those of chondrites (the chondritic ratio is 38) [33], but the Zr/Hf ratio of G4 granite clearly deviates from these values. Breiter et al. [34] proposed categorizing granites into common granites (Zr/Hf > 55), moderately evolved granites (25 < Zr/Hf < 55), and highly evolved granites (Zr/Hf < 25). It is evident that the G1-G3

 doi:10.20944/preprints202510.0931.v1

granites exhibit a composition that ranges from less to moderately evolved, whereas the G4 granite, characterized by a more highly evolved composition compared to the G1-G3.

Crystallization differentiation (i.e. mica, feldspars) induces a reduction in Nb/Ta and K/Rb ratios. However, fractional crystallization alone is insufficient to explain the occurrence of Nb/Ta<5 and K/Rb<150 in most peraluminous granites. It has been suggested that extremely low Nb/Ta and K/Rb ratios are further intensified by hydrothermal processes during the magmatic-hydrothermal transition, particularly in highly evolved granites [35].

The Nb/Ta ratios of Mesozoic peraluminous granites in the study area range from 0.89 to 6.11 (Table 5; Figure 11b), which intense deviate from the chondritic ratio (chondritic Nb/Ta = 17) [33]. If Nb/Ta ≤ 5 is taken as an indicator of hydrothermal processes [35], most Mesozoic granites predominantly fall within the magmatic-hydrothermal field. All studied granite samples exhibit low K/Rb ratios (< 150), indicating a highly evolved magma composition. The K/Rb ratio of magmatic rocks (230) is close to that of chondrites (242) [33], while most crust-forming rocks have K/Rb ratios ranging from 150 to 350 [36]. The G1 granite has the highest K/Rb ratios, ranging from 81.77 to 144.15, whereas the G2–G4 granites have lower and more widely varying ratios, ranging from 13.96 to 128.29 (Table 5; Figure 11b). Therefore, the low Nb/Ta and K/Rb ratios of the Mesozoic peraluminous granites result from both mineral crystallization fractionation and hydrothermal alteration during the late magmatic sub-solidus stage.

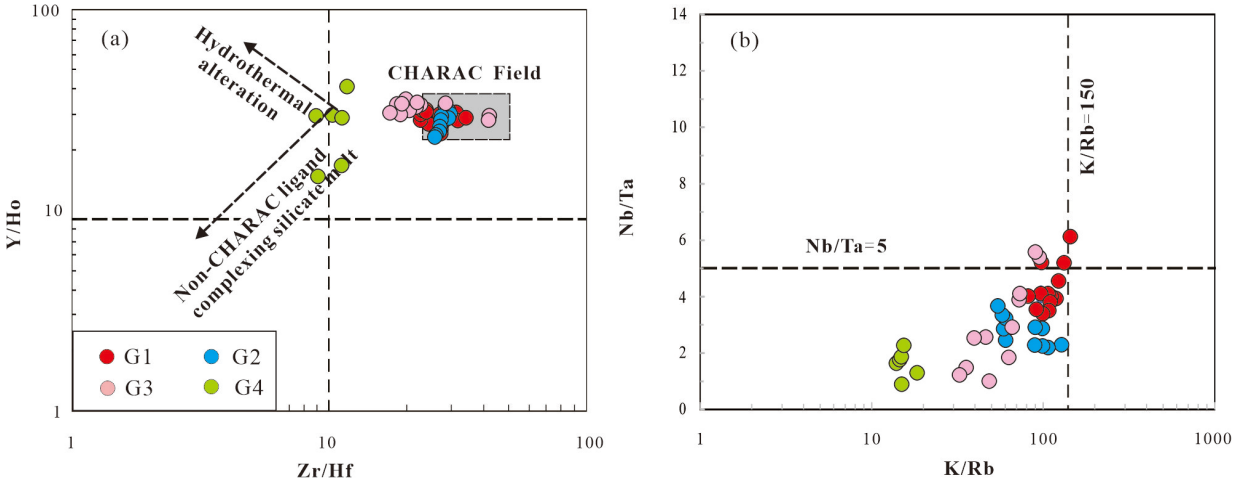

Figure 11. (a) Zr/Hf vs. Y/Ho ratios and (b) K/Rb vs. Nb/Ta ratios. Hydrothermal alteration and CHARAC field from [31].

Table 5. Rare-element contents of Mesozoic peraluminous granites in the Dahutang orefield.

	Nb/Ta	Zr/Hf	Y/Ho	K/Rb	W(ppm)	Cu (ppm)	Li (ppm)	Mo (ppm)	Nb (ppm)	Ta (ppm)	Sn (ppm)
G1 granite (n=14)											
Min	3.39	22.61	24.47	81.77	4.17	6.69	51.5	0.15	7.49	1.7	8.55
Max	6.11	34.13	31.52	144.15	86.8	1443	250	8.52	10.8	2.54	55.6
Mean	4.25	26.75	28.84	108.8	27.7	280.5	146.6	1.59	8.58	2.06	23.6
Median	4.01	26.50	29.10	108.26	27.2	146	155	1.00	8.54	2.01	23.6
G2 granite (n=11)											
Min	2.19	25.60	23.33	54.55	8.57	6.07	132	0.55	4.55	1.99	27.6
Max	3.66	29.96	32.32	128.29	1026	395	1243	7.19	19.6	6.71	310
Mean	2.75	27.94	28.54	82.23	121.4	175.5	334.8	2.20	13.6	4.97	86.7
Median	2.86	27.92	29.45	89.03	27.9	109	232	1.22	13.7	4.84	52.7
G3 granite (n=11)											
Min	1.00	17.31	28.71	32.71	20.3	11.2	225	0.59	17.2	3.16	34.9
Max	5.57	41.67	35.69	95.09	548	228	1050	12.2	34.6	27.4	251

 doi:10.20944/preprints202510.0931.v1

Mean	2.95	24.60	32.25	60.37	130.5	56.0	473.2	2.8	24.6	12.2	86.4
Median	2.56	20.53	33.23	63.07	76.1	32.7	321	1.4	24.3	9.5	75
G4 granite (n=6)											
Min	0.89	8.84	14.8	13.96	21.6	3.07	924	-	38.2	19.3	67
Max	2.26	11.64	41.4	18.44	801	98.6	2367	-	51.3	57.9	369
Mean	1.61	10.33	26.81	15.38	536	24.4	1739	-	43.9	30.5	186.6
Median	1.69	10.68	29.11	14.95	610	10.2	1829	-	43.4	25.2	119.5

5.5. Characteristics of ore-forming elements

Geochemical data reveal the following concentrations of ore-forming elements in the Mesozoic peraluminous granites of the study area: 4.17–801 ppm of W, 3.07-1443 ppm of Cu, 51.5-2367 ppm of Li, 0.15-12.2 ppm of Mo, 4.45-51.3 ppm of Nb, 1.7-57.9 ppm of Ta, 8.55-369 ppm of Sn (Table 5). Relative to the upper continental crust (UCC; values from [37]), the Mesozoic peraluminous granites exhibit strong enrichment in W, Sn, and Li, moderate enrichment in Ta and Cu, and comparable abundances in Sn and Nb. The enrichment sequence of metallogenic elements is: W > Sn > Li > Ta > Cu > Mo > Nb.

On ore-forming element box plots, the G1 granite are characterized by lower abundances of all rare metals, with the exception of Cu. The G2-G4 granite are enriched in W, Li, Sn, Ta and Nb relative to the less G1 granites, with their contents increasing progressively from G2 to G4 granite. G4 granite show significantly enriched abundances of W, Li, Sn, Ta and Nb compared to the G1, G2, and G3 granites (Figure 12). In contrast, Cu content shows an inverse trend: G1> G2> G3 > G4 granite. Nb content is slightly below UCC in G1 (8.58 ppm).

Using Σ(Fe + Mg + Ti) as a fractionation indicator, where decreasing Σ(Fe + Mg + Ti) indicates increasing degrees of fractionation or a variable source [38], ore-forming elements exhibit distinct behaviors between the G1 granite and the G2-G4 granites (Figure 12), which is analogous to the variation pattern of major elements. Nb, Ta, and P increase with fractionation in G2-G4 granites, but remains constant in G1granite. W and Sn are significantly elevated in the G2-G4 granite series relative to G1 granite. Mo shows decreases with fractionation in G1 granite, but increases in G2-G4 granites. Cu shows decreases with fractionation in G1 and G2-G4 granite series. It is evident that the G1 granite and the G2-G4 granites have distinct sources, and the differentiation of the two exerts different influences on ore-forming elements. For W, and Sn, differentiation is conducive to the enrichment of these elements—the higher the degree of differentiation, the greater the enrichment. For Cu, however, differentiation is unfavorable to mineralization, particularly in the G2-G4 granites. As for Li, Nb and Ta, the situation is more complex, with their behaviors varying across different rock types.

 doi:10.20944/preprints202510.0931.v1

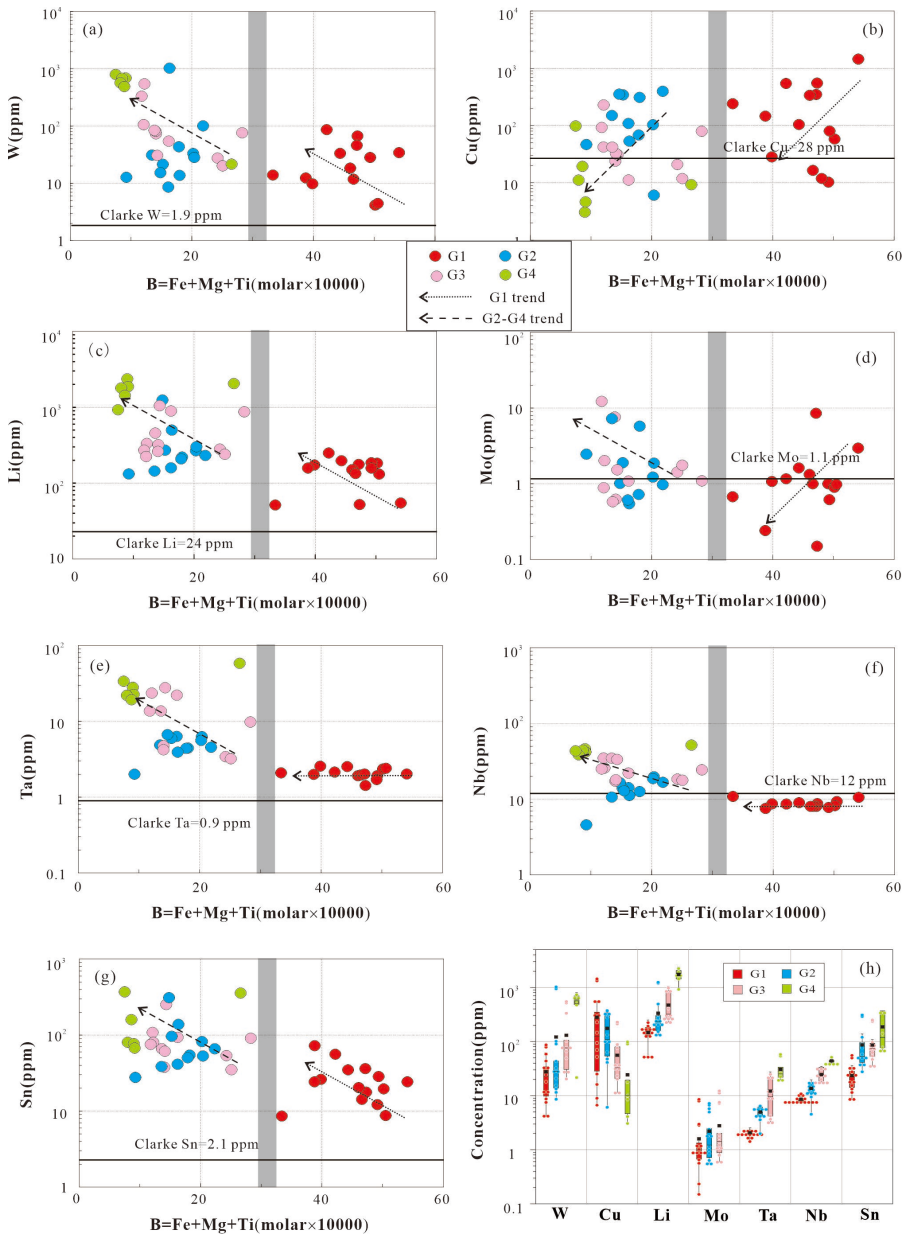

Figure 12. (a-g) Ore-forming elements versus the differentiation index plot [38] and (h) box plots of concentrations in ore-forming elements. Clarke values for the upper continental crust are shown as thick black lines (values from [37]).

6. Discussion

6.1. Spatio-temporal distribution of the Mesozoic peraluminous granites

In the Dahutang ore concentration area, substantial chronological and petrological studies have established a basic consensus that the magmatic activity in this region occurred within the time frame of 130-150 Ma. However, debates persist regarding whether this represents a prolonged single magmatic event or two-stage magmatic activities. We collected recently reported precise ages of the Mesozoic granites as well as the mineralization ages for cross-validation (Table 6, Figure 13). Although only a limited number of mineralization ages were available, the diagenetic ages were screened using the following criteria: U content is less than 3000 ppm; each dataset includes at least 15 effective analytical points; and for the same lithology in a single article, the data with the highest testing accuracy are selected. The Mesozoic peraluminous are divided into two periods: 147-152 Ma and 130-144 Ma. Existing mineralization dating efforts have predominantly centered on two time

 doi:10.20944/preprints202510.0931.v1

intervals, ~150 Ma and 139-144 Ma (Table 6 and Figure 13), which is consistent with magmatic activities.

We have noticed that despite the rigorous selection of age data, the errors in the age data of the two episodes still show systematic differences: the errors of the diagenetic ages of the G1 granite (147-152 Ma) and its associated mineralization ages (~150 Ma) are relatively small, while the errors of the diagenetic ages of the G2-G4 granites (130-144 Ma) and their associated mineralization ages (139-144) Ma are relatively large. The large age errors of the extensive G2-G4 magmatic stage are attributed not only to the limitations of analytical precision but also potentially to the recrystallization of dated minerals caused by magmatic-hydrothermal processes, which results in scattered ages and relatively large errors [42].

147-152 Ma magmatic activity is characterized by a single lithology (primarily G1), narrow geochemical and time range, implying limited magmatic differentiation; whereas 130-144 Ma magmatic activity consists of complex lithologies (including G2, G3, and G4), and shows diverse compositions and higher-degree evolution in a longer time span. So, though the emplacement of the G1 granite coincides spatially with that of the G2-G4 granites, it is noteworthy that these two episodes of magmatism are not genetically related and evolved independently.

Table 6. The ages of petrogenesis and mineralization in the Dahutang ore concentration area and its surrounding areas.

Deposit		Lithology or ore body	Age	MSWD	Mineral and method	Reference
Shimensi mining area	petrogenesis age	Porphyritic biotite granite	147.4±0.6	1.3	Zircon U-Pb	[7]
		Porphyritic biotite granite	149±1	1.7	Monazite U-Pb	[9]
		Biotite granite	150±0.7	1.6	Monazite U-Pb	[9]
		Porphyritic granite	143.1±1.2	0.4	Zircon U-Pb	[7]
		Porphyritic biotite granite	148.2±1.2	2.2	Monazite U-Pb	[9]
	mineralization age	Quartz vein type	139.2±1.0	2.9	Molybdenite Re-Os	[39]
		Quartz vein type	143.7±1.2	0.8	Molybdenite Re-Os	[40]
		Quartz vein type	149.6±1.2	1.6	Molybdenite Re-Os	[4]
Dawutang mining area	petrogenesis age	Granite porphyry	130.7±1.1	0.5	Zircon U-Pb	[6]
		Muscovite granite	133.7±0.5	0.5	Zircon U-Pb	[6]
		Muscovite granite	142.7±1.0	1.1	Monazite U-Pb	This paper
		Two-mica granite	140.3±1.0	1.5	Monazite U-Pb	This paper
		Granite porphyry	140.3±1.9	0.4	Zircon U-Pb	This paper
		Granite porphyry	130.3±1.1	2	Zircon U-Pb	[6]
		Granite porphyry	134.6±1.2	1.8	Zircon U-Pb	[5]
Shiweidong mining area	petrogenesis age	Porphyritic two-mica granite	144±0.6	0.2	Zircon U-Pb	[6]
		Porphyritic two-mica granite	136.6±1.0	1.4	Monazite U-Pb	This paper
	mineralization age	Quartz vein type	140.9±3.6	2.3	Molybdenite Re-Os	[40]
		Fine vein immersion type	142.4±8.9	1.7	Scheelite Sm-Nd	[8]
Kunshan mining section	petrogenesis age	Porphyritic biotite granite	149.5±0.9	0.3	Monazite U-Pb	This paper
		Porphyritic biotite granite	151.4±1.4	1.2	Monazite U-Pb	This paper
		Porphyritic granite	151.7±1.3	1.6	Zircon U-Pb	[16]
		Granite porphyry	136.6±2.5	3.8	Zircon U-Pb	[16]

 doi:10.20944/preprints202510.0931.v1

	mineralization age	Quartz vein type	150.0±1.0	0.3	Molybdenite Re-Os	[16]
Meizikeng mine spot	mineralization age	Quartz vein type	150.0±1.0	0.7	Molybdenite Re-Os	[41]

Statistical principles of petrogenesis age: ①U content is less than 3000 ppm; ②no less than 15 effective analysis points for each data; ③select the data with the best test accuracy for the same lithology in an article.

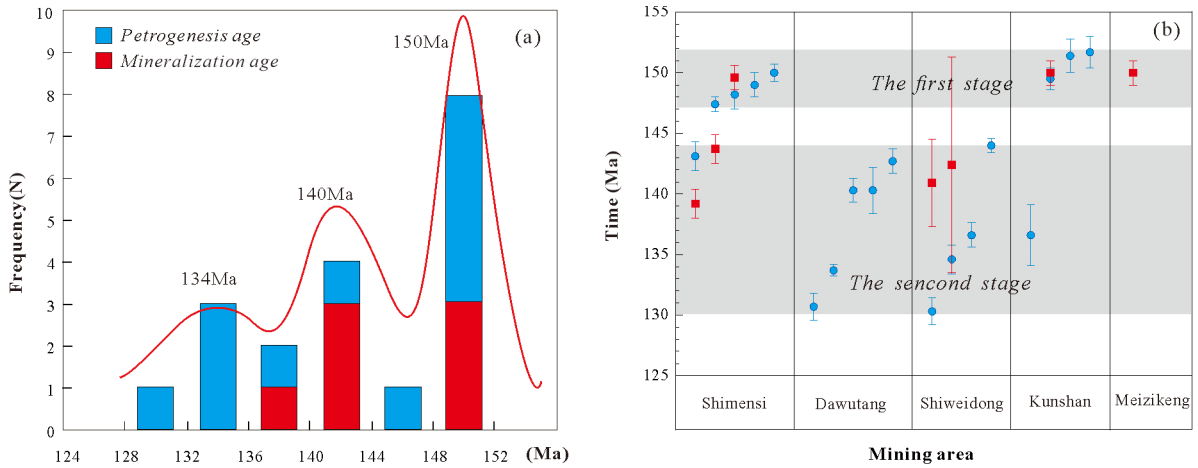

Figure 13. Histogram of ages of the Mesozoic granite and related ore deposits in the Dahutang District (the sources of the age data in the plots are listed in Table 3).

6.2. Implications for magma temperature

Zircon saturation thermometry (TZr) [43] provides a simple and robust means of estimating magma temperatures. Among all granites, G1 biotite granites have the highest zircon content (100-129 ppm), with calculated T_{Zr} values between 754 and 795°C (avg. 766°C) for 14 values (Table 4). Next is G2, where 11 samples have zircon contents of 49.7-98.3 ppm and calculated T_{Zr} values of 705-760°C (avg. 730°C). Third is G3 granite, which exhibits the widest temperature variation range: 11 samples have zircon contents of 31.2-124 ppm and calculated T_{Zr} values of 678-775°C (avg. 718°C). The G4 has the lowest temperature, with 6 samples showing zircon contents of 20.6-41.4 ppm and T_{Zr} values of 645-693°C (avg. 662°C). Among them, the highly fractionated G4 granite and a few G3 granites, with Zr <45 ppm, severe and obvious depletion of Sr, Eu, and Ba, exhibit lowest saturation temperatures, and their Zr/Hf ratios show obvious non-CHARAC behavior. Their T_{Zr} values represent only the minimum estimate of temperature rather than the initial magma temperature. 2) Excluding samples of Zr< 45 ppm, the average temperature of G3 granite is 735°C, which is essentially consistent with the temperature of G2 granite (730°C) and differs by 30°C from that of G1 biotite granite 766°C. So, ~766°C and ~735°C reflect the initial magma temperature of G1 granite and G2-G4 granites respectively.

Magma with a temperature of < 800 °C was defined as "cold magma" by Miller, C.F. [44]. At such a low temperature, mafic minerals and calcic plagioclase are highly insoluble, and melts are near Ab-Or-Qz minimum melt compositions. As a result, the magma contains a large number of residual minerals from the source area, making it almost impossible for the magma to erupt. All current models for generating large-scale magmas at T< 800°C within the crust require a source of water-rich fluid, because anhydrous melts require unrealistically high temperatures, and fluids could ascend into the zone of melting as a consequence of dehydration of underthrust sedimentary rocks or of hydrous mafic silicates in ultramafic-mafic rocks (cf. Thompson, 2001[45]; Patin˜o Douce, 1999[46]; Spear, 1995[47]). In conclusion, it is possible that the dehydration melting of subducted sedimentary rocks in a thickened crust environment gave rise to the low-temperature, high-silica peraluminous, and cryptic granites in the study area.

 doi:10.20944/preprints202510.0931.v1

6.3. Tectonic setting and metallogenic materials

Though the Mesozoic granites exhibit a strongly peraluminous feature (A/CNK >1.1; Figure 9c), they also possess calc-alkaline affinities and low Zr+Nb +Ce+Y contents (<200 ppm) (Figure 14a), distinguishing them from the diagnostic features of A-type granites [48]. Secondly, the studied granites exhibit apparently lower zircon saturation temperatures (<800℃; Table 4) compared with the typical A-type granites (>820℃). The fractionation of apatite is regarded as one distinctive feature for I- and S-type granites (e.g., Taylor andFallick, 1997[49]; Li et al., 2007[50]). G2-G4 granites have high P2O5 contents (mostly >0.2%, albite granite reaches up to 0.75%), and increases with the increase of fractionation in granites (Figure 12h), indicating that they have S-type affinity. But G1 granite with relatively low P_2O_5 contents (0.13%-0.2%) is more similar to the characteristics of I-type granite.

Sylvester [51] divided the source rock compositions of strongly peraluminous granites into psammite- and pelite-derived melt based on the CaO/Na_2O value of 0.3 as the boundary. G2-G4 granites are characterized by low CaO/Na_2O values (0.06-0.30), high Rb/Sr (8.1-382.2) and Rb/Ba ratios (1.9-3237; Figure 14b, 14c), which are similar to the compositions of the Himalayan strongly peraluminous granites. This indicates that they originated from the melting of upper crustal sediments with a high clay component. G1 granite is characterized by relatively high CaO/Na_2O value (0.31-0.57), low Al_2O_3/TiO_2 value, and low Rb/Sr (1.5-5.2) and Rb/Ba ratio (0.54-2.25). The samples are concentrated near the mixing line of basalt melt and pelite melt (Figure 14b, 14c), which are the products of the mixing of a small amount of basaltic rocks and clay-rich pelitic sediments, showing the characteristics of crust-mantle mixing. The mantle-derived signatures are primarily hosted in the G1 magmas as their elevated thermal state facilitates partial melting of crustal mafic minerals and calcic plagioclase, whereas the G2-G2 magmas exhibits lower and progressively decreasing temperatures, and melt compositions approaching the Ab-Or-Qz minimum. Previous studies [52-53, 13, 22] on the Nd-Hf-O isotopes of the Dahutang Mesozoic granite have also shown that these granites are mainly derived from partial melting of the Proterozoic crust (G2-G4) with minor mantle inputs (G1).

The field relationships, mineralogy and geochemistry data help to define the geodynamic setting of the Mesozoic peraluminous granites. The present study shows that the Mesozoic peraluminous granites is undeformed and unmetamorphosed. It represents the youngest igneous activity in the study area and intruded the subduction-related rocks. These criteria indicate a post-collisional setting for the Mesozoic peraluminous granites. Also, the chemical characteristics of the Mesozoic peraluminous granites are consistent with a post-collisional tectonic setting: marked depletion in Sr, MgO, CaO, and transition metals, primitive mantle-normalized patterns (Figure 10) enriched in both LILE and HFSE, and no depletion (quite the opposite, in fact) in Nb or Ta. On the tectonic discrimination diagram (Figure 14d, 14e), all granites fall within the collisional region, indicating they formed in a post-collisional environments.

Shuangqiaoshan Group in the eastern Jiangnan Orogen is formed in a back-arc basin associated with NW-dipping Neoproterozoic oceanic plate subduction beneath the Yangtze Block (Figure 1b) [55]. Plausibly, fluids could ascend into the zone of melting as a consequence of dehydration of subduction-related Shuangqiaoshan Group. W-Sn-Li-Nb-Ta partitions strongly into muscovites, which are often the first minerals involved in incongruent melting reactions. If metapelite source micas are also enriched in W-Sn-Li-Nb-Ta, any W-Sn-Li-Ta that is not partitioned into residual minerals during melting will be released to the resultant melt [56, 57]. In fact, Shuangqiaoshan Group are enriched in ore-forming metals, with W, Sn, Cu, Mo, and Ta contents of 10.1, 5.1, 38.5, 2.6, and 36-76 ppm, respectively [58-60], which are one to two orders of magnitude higher than the UCC. One of the reasons for the low Nb content in Mesozoic granites is the low Nb content of the Shuangqiaoshan Group (8-12 ppm, a little lower than UCC); low melting temperature is also an important contributing factor. The host minerals of Nb include muscovite, as well as biotite and Fe-Ti oxides (e.g., Stepanov & Hermann, 2013 [61]); in a low melting temperature, these minerals do not melt and cause Nb to partition into residual biotite and Fe-Ti oxides.

 doi:10.20944/preprints202510.0931.v1

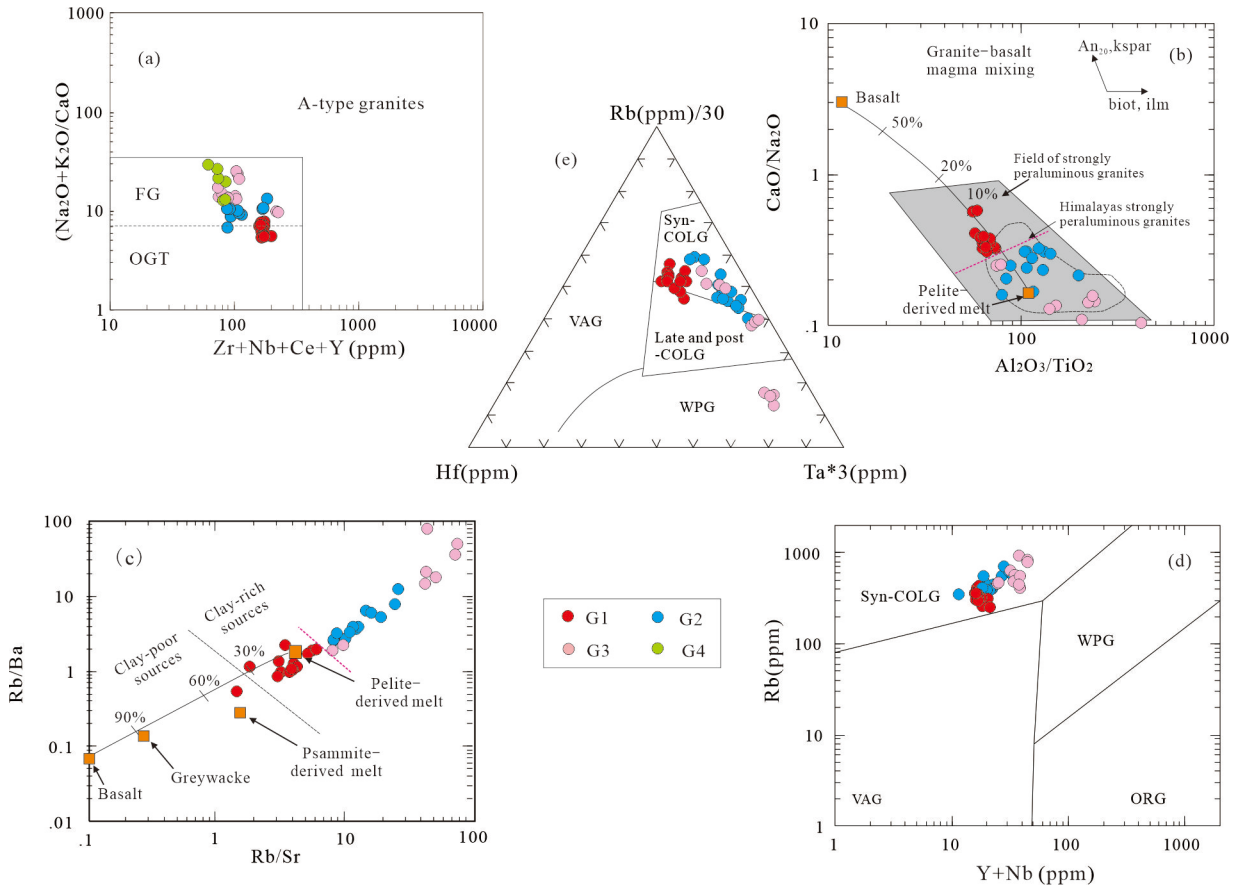

Figure 14. (a) (K2O+Na2O)/CaO- Zr+Nb+Ce+Y [48], (b) CaO/Na2O- Al2O3/TiO2 [51], (c) Rb/Sr- Sr/Ba [51], (d) Rb-(Y+Nb), and (e) Rb-Hf-Ta*3 [54]. FG: fraetionated felsic granites; OGT: unfractionated M-, I- and S-type granites; An20: Vectors for fractional crystallization of oligoclase; kspar: K-feldspar; biot: biotite; and ilm: ilmenite; syn-COLG: Syn-collisional; VAG: volcanic arc; WPG: within-plate; ORG: oceanic ridge; Late and post-COLG: Late and post-collisional.

6.4. The role of fluorine and phosphorus

Although F was not analyzed in this study, it emerges as a key control on the distribution of W, Sn, Nb, Ta in peraluminous Mesozoic granites. Based on previous data, F content shows a moderate increase from approximately 0.1%-0.69% in G2 granites to 0.21%-0.84% in G3-G4 granites [13]. Elevated F is typical of fractionated peraluminous melts; together with other fluxing elements (e.g. P, Li, B), it lowers the melt temperature and reduced viscosity [62]. High F concentrations promote the retention of W, Sn, Li, Nb and Ta in low-temperature melts, with these metals preferentially partitioning into the melt during its evolution. This pattern is observed in the G4 granites, which have the highest F contents, also exhibit the highest W, Sn, Li, Nb and Ta concentrations (Figure 12). No relevant data on F in G1 granites was identified.

Like F, phosphorus accumulates with the fractionation of peraluminous melts, reaching maximum levels in the most evolved granites which also have the lowest Ca contents. When P is present in high concentrations alongside low Ca, a relationship designated the "Pedrobernardo-type" trend by Bea et al. (1992) [63], P exhibits the behavior of an incompatible element and concentrates in residual fluids. This phenomenon arises because limited Ca availability constrains apatite crystallization. Within G2-G4 granites, P_2O_5 shows a positive correlation with Rb, commonly enriched in residual melts and a negative correlation with compatible elements such as Sr and Ba (Figure 10). Extending this relationship to rare metals: in G2-G4 S-type granites, P_2O_5 correlates positively with W, Sn, Li, Nb, Ta, and Mo, and negatively with Cu, while no overall trends with Mo; for G1 I-type

 doi:10.20944/preprints202510.0931.v1

granites, W, Cu, Li and Sn show no overall trends, while Nb and Ta exhibit a little positive correlation (Figure 15). The combined effects of F and P, along with Li, favor the retention of W, Sn, Nb, Ta, with no such effect on Cu and Mo in the S-type granitic melt. This enhances the potential for these metals (W, Sn, Nb, Ta) to later partition into exsolving magmatic-hydrothermal fluids. However, in I-type granites fluxing elements have almost no such effect.

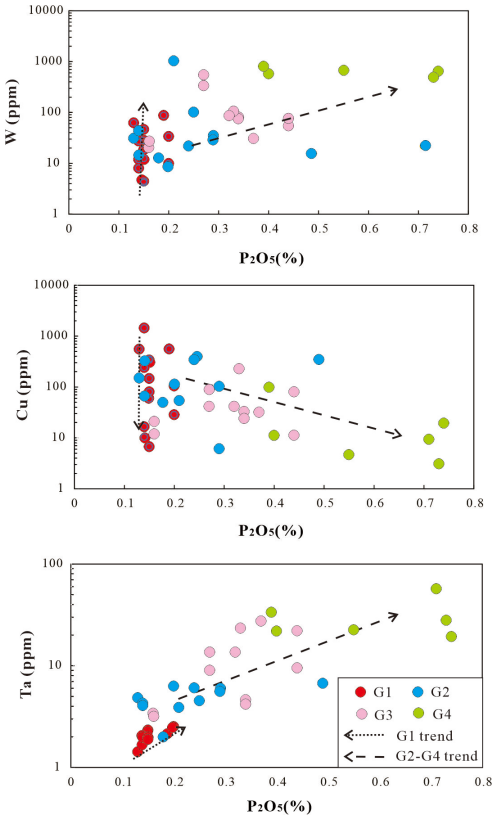

Figure 15. Trace element variation diagrams with P_2O_5 (%) as the abscissa. P_2O_5 becomes concentrated in residual fluids during evolution of peraluminous granites and correlations for a) P_2O_5-W, b) P_2O_5-Cu, and c) P_2O_5-Ta indicate whether these metals concentrated in residual fluids.

6.5. PH, Eh conditions as indicators of mineralisation

Redox state controls the efficiencies of removal of metal from source into the melt, partition coefficients of metal species to coexisting melt, and transportation of metal into ore-forming fluid [64]. An empirical redox indicator is the whole-rock Fe_2O_3/FeO ratio (e.g., Blevin, 2004 [65]). The G1 granite exhibits Fe_2O_3/FeO ratios ranging from 0.04 to 1.47 (avg. 1.07)： the 7 samples of the Shimensi mining area range from 1.27 to 1.47 , whereas 3 samples of the Kunshan mining area exhibit significantly lower ratios (0.04-0.14) (Table 4, Figure16a and 16b). Most samples reflecting an oxidized redox state and relatively high oxygen fugacity and correspond to the magnetite series as defined by Ishihara (1981)[66]. The G2-G4 granites characterized by Fe_2O_3/FeO ratios of 0.04-0.47 (avg. 0.19), reflect a reduced redox state and low oxygen fugacity, consistent with the ilmenite series (Table 4, Figure16a, 16b). Nevertheless, as pointed out by Blevin (2004) [65], for granitic rocks featuring high SiO_2 contents (>72%) and low total FeOT (<2%), the Fe_2O_3/FeO ratios is unsuitable to reveal the magmatic oxygen fugacity. It is necessary to employ alternative methods for determining the redox state.

Previous experimental studies have demonstrated that there is a certain correlation between the contents of FeO and MnO in wolframite and the pH, Eh conditions of formation [67-69]. Wolframite (Fe, Mn)WO_4 is an intermediate member of the complete isomorphous series of ferberite ($FeWO_4$)-hübnerite ($MnWO_4$). In a weakly acidic and oxidative environment, iron ions exist as Fe^{3+} rather than Fe^{2+}; this state is unfavorable for their combination with WO_4^{2-}, but more favorable for Mn^{2+} to

 doi:10.20944/preprints202510.0931.v1

combine with WO_4^{2-} and form $MnWO_4$. Consequently, the $MnWO_4/FeWO_4$ ratio is greater than 1. However, in a weakly alkaline and reductive environment, iron ions in the fluid exist as Fe^{2+} rather than Fe^{3+}; Mn^{2+} is gradually replaced as Fe^{2+} combines with WO_4^{2-} to form $FeWO_4$, resulting in a $MnWO_4/FeWO_4$ ratio of less than 1. For the wolframite of G1 granite, the $MnWO_4/FeWO_4$ ratio ranges from 0.31 to 0.73 (avg. 0.42): Shimensi mining area of 0.32-0.73 (average 0.48); Kunshan mining area of 0.31-0.46 (avg. 0.35). For the wolframite of G2 granite, the $MnWO_4/FeWO_4$ ratio ranges from 0.16-0.39 (avg. 0.25): Dawutang mining area of 0.17-036 (avg. 0.24); Shiweidong mining area of 0.19-039 (avg. 0.26). The $MnWO_4/FeWO_4$ ratios of all wolframite are less than 1, indicating they are ferromanganese wolframite and formed in a generally weakly alkaline and relatively reducing environment. However, the $MnWO_4/FeWO_4$ ratio in the G1 granites is much higher than that in the G2 granites, especially in the Shimensi mining area (Figure 16c). It indicates that wolframite crystallized in two periods under different environments.

Based on the geochemical characteristics of whole rocks and wolframite, the magmas of both G1 granite and G2-G4 granites are generally in a reduced redox state, but there are still obvious differences between them. The G2-G4 granitic magmas exhibit strong reducibility, which increases with the rise of Rb/Sr ratio from G2 to G4. In contrast, the G1 granite lies between the reduced and oxidized redox states. The reason why G1 granite magma is more oxidative than G2-G4 granite magmas may be that there was an injection of minor mantle materials into its magmatic source area.

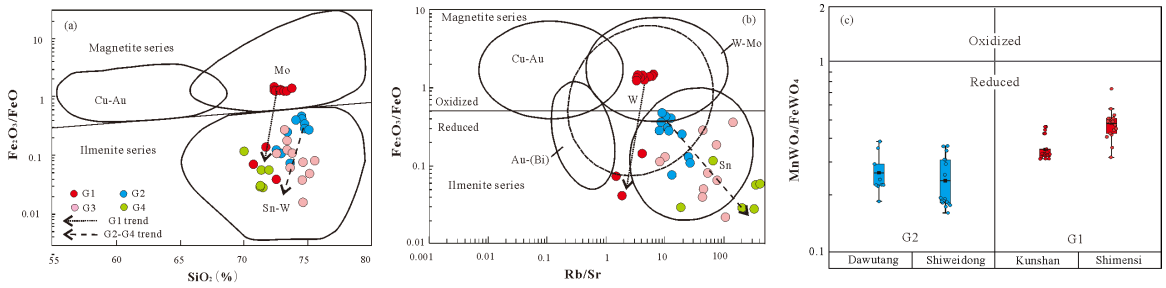

Figure 16. (a) Fe_2O_3/FeO vs. SiO_2 diagram (field boundaries are after [66]); (b) Fe_2O_3/FeO vs. Rb/Sr diagram (field boundaries are after [70, 71]); (c) Box plots showing the range of $MnWO_4/FeWO_4$ ratio of wolframites.

The magmatic redox state can play an important role in determining the types of ore deposits produced from magmatic melts by affecting the enrichment processes of the metals. Cu and Mo are sulphophile elements, and its mineralization is generally associated with oxidized magmas [64, 72-73], whereas reduced redox state is beneficial for Sn-Li-Nb-Ta mineralization (Figure 16a, 16b; e. g., Linnen et al., 2005 [74]; Zaraisky et al., 2010[75]). W seems to show little dependence on magmatic redox state because it dissolves predominantly as W6+ at all oxygen fugacities in silicate magma [76]. However, lower oxygen fugacity is favorable for the removal of tungsten from magma into hydrothermal ore-forming fluids [77-78]. We infer that the G1 magmas have potentials to form minor Cu and Mo mineralization whereas the G2-G4 magmas are favorable for significant W-Sn-Li-Nb-Ta.

6.6. Magmatic evolution, hydrothermal alteration and mineralization

More than one genetic hypothesis have been proposed for the origin of the Mesozoic peraluminous granites in the Dahutang area: (1) melt-fluid interaction origin [12], (2) fractional crystallization origin [15, 23], and (3) a combination of melt-fluid interaction with fractional crystallization origin [13].

Both of G1 granite and G2-G4 granites represent different stages of fractionation and late stage fluid-melt interactions which are shown by many geologic, petrographic and chemical observations. Geologically, The formation of hydrothermal cryptoexplosive breccia pipe, pegmatitoid, greisen, and quartz veins in Dahutang area indicates that the parent melts were volatile saturated. Petrographically, exsolution textures represented by perthites, rhythmic zoning of Plagioclase, as well as the turbidity of alkali-feldspars observed in both of them characterize the highly fractionated

 doi:10.20944/preprints202510.0931.v1

granites [79-81]. Geochemically, CaO, TiO_2, Sr depletion and higher Al_2O_3 and Na_2O in addition to the strong negative Eu anomalies can be reflect extensive fractionation of biotite and plagioclase, while low Ba can interpret the K-feldspar fractionation [82] and this is compatible with albite dominance in G2-G4 granites and orthoclase in G1 granite. Both of G1 granite and G2-G4 granites show significant evidence of interaction with fluids, i.e. high contents of Sn (30-10000 ppm), Cs (35-1000 ppm), F (>0.4%-4%), Li (250-2000 ppm), W (10-1000 ppm) and Rb (>500 ppm), with low Nb/Ta (<5) [35]. Because such incompatible elements have a strong affinity for magmatic fluids, their enrichment is commonly used as a marker of a magmatic-hydrothermal alteration in evolved crustal granites.

Nb/Ta of G1 granite ranges from 3.39-6.11 whereas G2-G4 samples have lower Nb/Ta ratios (0.89-3.66). Figure 17 illustrates the melt evolution model proposed by Ballouard C [35]. Those modeling qualitatively reproduces the behaviors of Nb and Ta. According to this model, G1 granite and G2-G4 granites exhibit two distinct mineral fractionation trends in terms of Fe-Ti oxides and micas, respectively. However, both show a high degree of fractionation, ranging from 75% to 90%, to reach low Nb/Ta ratios of 2~4. This unrealistic degree of fractionation suggests the involvement of hydrothermal processes as well. For this reason, the extensive decrease of the Nb/Ta whole-rock values in G2-G4 granites may be enhanced by late magmatic fluids causing secondary muscovitization process [35].

In the G1 granite, the K/Rb-ratios vary between 81.77 and 144.15 whereas in the G2-G4 granites vary between 13.96 and 128.29. This lower ratio (<150), which is lower ratio than chondritic value (242) [33], indicates the interaction with an aqueous fluid phase [83] or growth of mineral in the existence of aqueous fluids [84] characterizing the evolved magmatic system. The Zr/Hf ratio of G1 granites range from 22.61-34.13 near to the Zr/Hf ratio of chondrite (38) [33] indicating that G1 may represent the stage of evolution corresponding to the beginning of fluid-melt interaction accompanied by fractionation of biotite and feldspars. Instead, the ratios of Zr/Hf of G2-G4 granites decrease strongly relative to chondrite indicating the later stage of evolution more affected by fluid-melt interaction. Based on the variation characteristics of the Y/Ho and Zr/Hf ratio (influenced solely by magmatic fluids) and the K/Rb and Nb/Ta ratios (influenced by both fractional crystallization and magmatic fluids), We infer that G1 granite represents moderately fractionated melt with the lower effect of magmatic melt-fluid interaction, and G2-G4 granites support intense crystal fractionation and the fluid-mobilization.

The Zr/Hf ratio serves as a geochemical proxy for the fertility of granitic rocks. Specifically, granites associated with Sn, W, Mo, Be, and Ta mineralization are anticipated to have a Zr/Hf ratio <30 (corresponding to the lower limit of CHARAC range; [31]), and this characteristic is illustrated in Figure 18a [85]. In Figure 18a, all the Mesozoic peraluminous granites in the Dahutang district have geochemical features distinct from those of barren granites, but similar to those of ore-bearing granites. Among these granites, the G1 granites, characterized by small variations in Zr/Hf ratio (20<Zr/Hf<35), are associated with Sn, W, Mo, and Be mineralization. In contrast, the G2-G4 granites exhibit a large range of Zr/Hf ratio (~10<Zr/Hf<45), which consequently enables them to have a broader mineralization potential—encompassing not only Sn, W, Mo, and Be but also Li and Ta mineralization. Similar, in a Nb/Ta versus Zr/Hf diagram (Figure 18b), the G1 granite fall into the field of Sn-W-(U)-bearing granites, while G2-G4 granitic series spans two zones: Sn-W-(U)-bearing granites and rare-metalbearing granites (Figure 18b).

From the perspective of the geochemical properties of elements, tungsten is a crust-loving element, while copper is a mantle-loving element. In the Dahutang orefield, U and Cu are closely associated, with U reaching a super-large scale and Cu reaching a medium-large scale. The cause of the rare metallogenic phenomenon of the close association between U and Cu has long been a subject of discussion (i.e.[5, 10, 24]). If the W-Cu association is a phenomenon formed in a single phase of magma, it is rare and difficult to explain. However, if they are products of different magmas, and only overlap in the ore-hosting space, this can be easily understood. From the diagrams presented in Figures 13, 14, and 16, we highlight significant chronological (147-152 Ma and 130-144 Ma),

 doi:10.20944/preprints202510.0931.v1

geochemical (I-type and S-type), redox state, and metallogenic (W-Cu-Mo and W-Sn-Li-Ta mineralization) evidence that each stage granite has its own discrete episodes of magmatism and mineralisation and there is not a all-time fluid source for the mineralisation. The G1 granite and G2-G4 granites have potentially exsolved differ metals and rare metals in differing relative proportions due to the variations source melting conditions and subsequent fractionation. Fractional crystallization and subsolidus hydrothermal alteration together have boosted the solubility and hydrothermal transport capacity of W-Sn-Li-Nb-Ta by multiple orders of magnitude—this effect occurs specifically in the G2-G4 magmas, which are reduced, rich in volatiles, and aqueous. In contrast, the G1 granite magma differs significantly: it is more oxidative and contains fewer volatiles than the G2-G4 suite. When intense crystal fractionation takes place, this G1 magma has the potential to generate W, Cu, and Mo mineralization. Mineral exploration efforts in the Dalutang mining area have, historically, centered mainly on W, Cu, and Mo. Our research, however, leads us to the conclusion that the region holds substantial mineral potential for rare metals—with Sn, Li, and Ta being the key ones. Looking ahead, future surveys ought to give priority to zones neighboring the evolved G2-G4 peraluminous leucogranites, as these areas are promising for discovering new concealed mineral deposits.

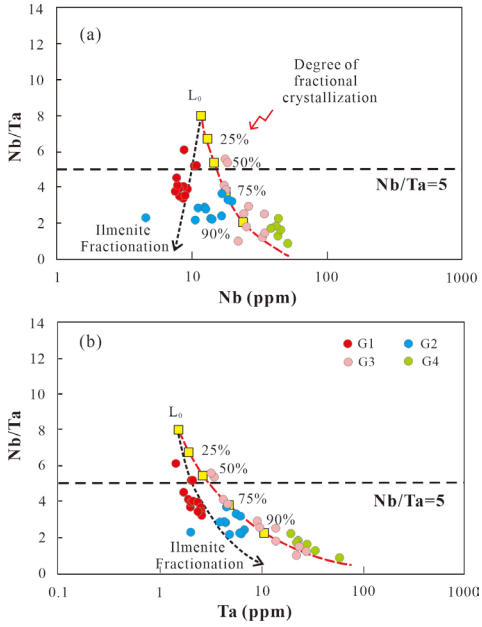

Figure 17. (a) Nb/Ta vs. Nb and (b) Nb/Ta vs. Ta diagram. Red curves represent model of evolution of Nb and Ta in liquid L0 (Nb=12 ppm, Ta=1.5 ppm, Nb/Ta = 8) during fractionation of assemblage made of 10% biotite + 10% muscovite + 80% (quartz + feldspar). Numbers above curves indicate amount of fractional crystallization. Black dashed line represents same model during fractionation of assemblage composed of 10% biotite + 10% muscovite + 0.5% ilmenite + 79.5% (quartz + feldspar). The melt evolution model proposed by Ballouard C [35].

 doi:10.20944/preprints202510.0931.v1

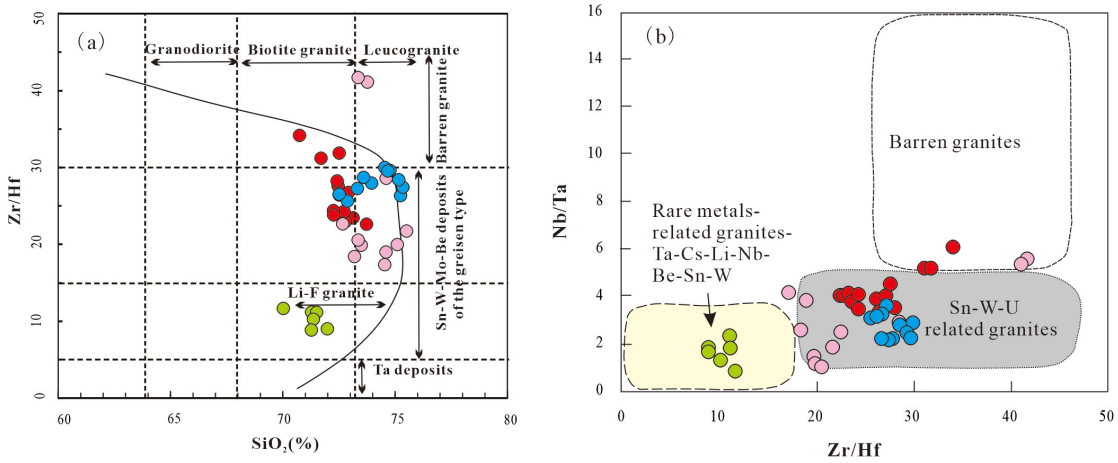

Figure 18. (a) SiO_2 vs. Zr/Hf [85] and (b) Zr/Hf vs. Nb/Ta diagram [35].

7. Conclusions

The Mesozoic peraluminous granites are composite, constructed over 20 Ma. An earlier magmatic stage (152-147 Ma) involved biotite melting of a Proterozoic subducted crustal source, with minor mantle contributions, generating biotite (G1) granites. Sustained collision induced lower-temperature, muscovite-dominated melting, leading to a second major magmatic episode (144-130 Ma) that produced two-mica (G2) granites. Subsequent fractionation yielded muscovite (G3) and albite (G4) granites. This crustal source, enriched in W, Sn, Li, Cu, Mo, and Ta, would have generated melts rich in these elements.

The G1 granite and G2-G4 granites are peralumineous rare metal bearing I- and S-type granites respectively, and formed by fractional crystallization accompanied by varied late magmatic fluid overprint. They share some similarities and greatly vary in other geologic, petrographical and chemical aspects. The G2-G4 granites are more evolved showing numerous evidences of late magmatic fluid-melt interaction as 1) hydrothermal cryptoexplosive breccia pipe, pegmatitoid, and quartz veins, 2) exsolution textures represented by perthites, 3) secondary albite overgrowth on the rim of K-feldspar, 4) rich fluxing elements (e.g. F, P, Li), 5) the low values of K/Rb, Nb/Ta, Zr/Hf and REE tetrad effect of G4 granite declare non-CHARAC behavior causing modification of magmatic trace element abundances by fluid-melt interaction. On the other hand, G1 granite shows few evidences of late-magmatic fluid-melt interaction as 1) hydrothermal cryptoexplosive breccia pipe, pegmatitoid, greisen, and quartz veins, 2) slight replacement of biotite by muscovite, chlorite and iron oxides, 3) K/Rb and Nb/Ta ratios that are lower than those of chondrites but higher than those of G2-G4 granites, 4) chondritic or closely chondritic Zr/Hf and Y/Ho ratios and absence of tetrad effect, indicating the lower imprint of late stage magmatic fluid-melt interaction than G2-G4 granites.

Zr saturation temperatures (< 800°C) indicate that these granites crystallized under shallow, low-temperature, water-rich conditions. In the reduced, volatile-rich aqueous G2-G4 magmas, the solubility and hydrothermal transport capacity of W-Sn-Li-Nb-Ta have been enhanced by multiple orders of magnitude under the combined influence of fractional crystallization and subsolidus hydrothermal alteration. But the G1 granite magma, which is more oxidative and less volatile than G2-G4 granite magmas, potentials to form W, Cu and Mo mineralization accompanied by intense crystal fractionation.

Author Contributions: Conceptualization, H.M.Y. and M.T.S.; methodology, H.M.Y.; formal analysis, H.M.Y. and L.Z.; investigation, H.M.Y. and C.S.W.; resources, H.M.Y. and M.G.Y.; data curation, H.M.Y.; writing—original draft preparation, H.M.Y.; writing—review and editing, H.M.Y. and M.T.S.; visualization, H.M.Y.; supervision, H.M.Y. and X.L.Z.; project administration, H.M.Y.; funding acquisition, H.M.Y. and M.G.Y. All authors have read and agreed to the published version of the manuscript.".

Funding: This research was funded by China Geological Survey Project (Grant No. DD202402081 and DD20240067), and National Natural Science Foundation of China (Grant No. 92062223).

Data Availability Statement: The original contributions presented in this study are included in the article. Further inquiries can be directed to the corresponding authors.

Acknowledgments: The study has benefited from discussions with Chuanlin Zhang and Xianhua Li. The manuscript benefitted greatly from critical reviews by anonymous reviewers.

Conflicts of Interest: The authors declare no conflicts of interest.

References

1. Bonin, B. Do coeval mafic and felsic magmas in post-collisional to within-plate regimes necessarily imply two contrasting, mantle and crustal, sources? A review. *Lithos* **2004**, *78*, 1–4.
2. Bonin, B. A-type granites and related rocks: evolution of a concept, problems and prospects. *Lithos* **2007**, *97*, 1–29.
3. Xiang, X.K, Chen, M.S., Zhan, G.N., Qian, Z.Y.i, Li, H., Xu, J.H. Metallogenic geological conditions of Shimensi tungsten-polymetallic deposit in north Jiangxi province. *Contrib. Geol. Miner. Resour. Res.* **2012**, *27*, 143–155.
4. Xiang, X.K., Wang, P., Sun, D.M., Zhong, B. Re-Os isotopic age of molybdeinte from the Shimensi tungsten polymetallic deposit in northern Jiangxi province and its geological implications. *Geol. Bull. China* **2013**, *32*, 1824–1831.
5. Huang, L.C., Jiang, S.Y. Geochronology, geochemistry and petrogenesis of the tungsten-bearing porphyritic granite in the Dahutang tungsten deposit, Jiangxi Province. *Acta Petrol. Sin.* **2013**, *29*, 4323–4335.
6. Huang, L.C, Jiang, S.Y. Highly fractionated S-type granites from the giant Dahutang tungsten deposit in Jiangnan Orogen, Southeast China: Geochronology, petrogenesis and their relationship with W-mineralization. *Lithos* **2014**, *202–203*, 207–226.
7. Mao, Z.H., Liu, J.J, Mao, J.W., Deng, J., Zhang, F., Meng, X.Y., Xiong, B.K., Xiang, X.K., Luo, X.H. Geochronology and geochemistry of granitoids related to the giant Dahutang tungsten deposit, middle Yangtze River region, China: Implications for petrogenesis, geodynamic setting, and mineralization. *Gondwana Res*. **2015**, *28*, 816–836.
8. Jiang, S.Y., Peng, N.J., Huang, L.C., Xu, Y.M.g, Zhan, G.L., Dan, X.H. Geological characteristic and ore genesis of the giant tungsten deposits from the Dahutang ore-concentrated district in northern Jiangxi Province. *Acta Petrol. Sin.* **2015**, *31*, 639–655.
9. Ye, H.M., Zhang, X., Zhu, Y.H. In-situ Monazite U-Pb Geochronology of Granites in Shimensi Tungsten Polymetallic Deposit, Jiangxi Province and its Geological Significance. *Geotect. Metallo*. **2016**, *40*, 58–70.
10. Sun, K.K., Chen, B., Deng, J. Biotite in highly evolved granites from the Shimensi W-Cu-Mo polymetallic ore deposit, China: Insights into magma source and evolution. *Lithos* **2019**, *350-351*, 105245.
11. Fan, X.K., Hou, Z.Q., Zhang, Z.Y., Mavrogenes, J., Pan, X.F., Zhang, X, Xiang X.K. Metallogenic ages and sulfur sources of the giantDahutang W-Cu-Mo ore field, South China: Constraints frommuscovite $^{40}Ar/^{39}Ar$ dating and in situ sulfur isotope analyses. *Ore Geol. Rev.* **2021**, *134*, 104141. Doi: 10.1016/j.oregeorev.2021.104141.
12. Zhang, Z.H., Zhang, D., Xiang, X.K., Zhu, X.Y., He, X.L. Geology and mineralization of the supergiant Shimensi granitic-type W-Cu-Mo deposit (1.168 Mt) in northern Jiangxi, South China: A Review. *China Geol.* **2022**, *5*, 510–527. doi: 10.31035/cg2022036.
13. Yang, Y.S., Pan, X.F., Hou, Z.Q., Deng, Y., Zhang, Z.Y., Fan, X.K., Li, X., Liu, D.W. Petrogenesis and redox state of late Mesozoic granites in the Pingmiao deposit: Implications for the W–Cu–Mo mineralization in the Dahutang district. *Ore Geol. Rev.* **2022**, *145*, 104898.
14. Li, X.H., Li, Z.X., Ge, W.C., Zhou, H.W., Li, W.X., Liu, Y., Wingate, M.T.D. Neoproterozoic granitoids in South China: crustal melting above a mantle plume atnca. 825 Ma? *Precambian Res.* **2003**, *122*, 45–83.
15. Sun, K.K., Chen, B., Chen, J.S., Xiang, X.K. The petrogenesis of the Jiuling granodiorite from the Dahutang deposit, Jiangxi Province and its tectonic implications. *Acta Petrol. Sin.* **2017**, *33*, 907–924.

16. Zhang, M.Y, Feng, C.Y., Li, D.X., Wang, H., Zhou, J.H., Ye, S.Z., Wang, G.H. Geochronological study of the Kunshan W-Mo-Cu Deposit in the Dahu-tang Area, Northern Jiangxi Province and its geological significance. *Geotect. Metallo.* **2016**, *40*, 503–516.
17. Xiang, X.K., Yin, Q.Q., Zhan, G.N., Qu, K., Liu, X., Tan, R., Zhong, B. Metallogenic conditions and ore-prospecting of Shimensi tungsten ore-section in the North of Dahutang Area in Jiangxi Province. *J. Jilin Univ. (Earth Sci. Edi.)* **2017**, *47*, 645–658. doi: 10.13278/j.cnki.jjuese.201703101.
18. Zhong, H., Yu, N.B., Lu, G.S., Chen, D.K., Dan, X.H. Discovery and Exploration Enlightenment of the Dawutang Extra Large Tungsten Deposit in the Jiangnan Tungsten Mine Belt. *South China Geol.* **2024**, *40*, 343–352.
19. Ludwig, K.R. User's manual for Isoplot/Ex (rev. 2.49): a geochronological toolkit for Microsoft excel. Berkeley Geochronology Centre: Special Publication 2001; No. 1a, pp. 55.
20. Ивойлов А.С., Qiu, Y.Z. Supplementary information of the form of niobium tantalum in the black tungsten deposit. *Geol. Geochem.* **1974**, *7*, 20–21.
21. Zhang, C.Z. Variation in Nb-Ta contents of wolframite and its significance as an indicator. *Miner. Deposi.* **1984**, *3*, 59–67.
22. Huang, L.C., Jiang, S.Y. Highly fractionated S-type granites from the giant Dahutang tungsten deposit in Jiangnan Orogen, Southeast China: geochronology, petrogenesis and their relationship with W-mineralization. *Lithos* **2014**, *202–203*, 207–226.
23. Jiangxi Bureau of Geology and Mineral Exploration and Development northwest Jiangxi Brigade. Verification report of tungsten ore resources and reserves in Dawutang mining area, Jing'an County, Jiangxi Province, China, 2016; No published.
24. Yang, Y.S., Pan, X.F., Hou, Z.Q., Deng, Y., Zhang, Z.Y., Fan X.K., Lia, X, Liu, D.W. Petrogenesis and redox state of late Mesozoic granites in the Pingmiao deposit: Implications for the W–Cu–Mo mineralization in the Dahutang district. *Ore Geol. Rev.* **2022**,*145*,104898. https://doi.org/10.1016/j.oregeorev.2022.104898.
25. Le Maitre, R.W., Bateman, P., Dudek, A., Keller, J., Lameyre, J., Le Bas, M.J., Sabine, P.A., Schmid, R., Sorensen, H., Streckeisen, A., Wooley, A.R., Zanettin, B. In *A classification of igneous rocks and glossary of terms*; Blackwell, Oxford, 1989; pp. 193.
26. Sylvester, P.J. Post-collisional alkaline granites. *J. Geol.* **1989**, *97*, 261–280.
27. Maniar, P.D., Piccoli, P.M.. Tectonic discrimination of granitoids. *Geol. Soc. Amer. Bull.* **1989**, *101*, 635–643.
28. Stanley, C.R. Molar element ratio analysis of lithogeochemical data: a toolbox for use in mineral exploration and mining. *Geochemistry: Exploration, Environment, Analysis* **202**0, *20*, 233–256.
29. Harlaux, M., Blein, O., Ballouard, C., Kontak, D.J., Thi´eblemont, D., Dabosville, A., Gourcerol, B. Geochemical footprints of peraluminous rare-metal granites and pegmatites in the northern French Massif Central and implications for exploration targeting. *Ore Geol. Rev.* **2025**, *176*, 106409.
30. Sun, S.S., McDonough, W.F. Chemical and isotopic systematics of oceanicbasalts: Implications for mantle composition and processes. *Geol. Soc. Lond. Spec. Publ.* **1989**, *42*, 313–345.
31. Bau, M. Controls on the fractionation of isovalent trace elements in magmatic and aqueous systems: evidence from Y/Ho, Zr/Hf, and lanthanide tetrad effect. *Contrib. Mineral. Petrol.* **1996**, *123*, 323–333. https://doi.org/10.1007/s004100050159.
32. Irber, W. The lanthanide tetrad effect and its correlation with K/Rb, Eu/Eu*, Sr/Eu, Y/Ho, and Zr/Hf of evolving peraluminous granite suites. *Geochem. Cosmochim. Acta* **1999**, *63*, 489–508. https://doi.org/10.1016/s0016-7037(99)00027-7.
33. Anders, E., Grevesse, N. Abundances of the elements: meteoritic and solar. *Geochem. Cosmochim. Acta* **1989**, *53*, 197–214.
34. Breiter, K., Skoda, R., Uher, P. Nb-Ta-Ti-W-Sn oxide minerals as indicators of a peraluminous P- and F-rich granitic systems evolution: Podlesi, Czech Republic. *Mineral. Petrol.* **2007**, *91*, 225–248.
35. Ballouard, C., Poujol, M., Boulvais, P., Branquet, Y., Tart`ese, R., Vigneresse, J. Nb-Ta fractionation in peraluminous granites: a marker of the magmatic-hydrothermal transition. *Geology* **2016**, *44*, 231–234.
36. Taylor, S. The application of trace element data to problems in petrology. *Phys. Chem. Earth* **1965**, *6*, 133–213.

 doi:10.20944/preprints202510.0931.v1

37. Rudnick, R.L., Gao, S. Composition of the Continental Crust. *Treatise on Geochemistry*, **2014**, *2Nd Edition* 4, 1–51. https://doi.org/10.1016/B978-0-08-095975-7.00301-6.
38. Debon, F., Le Fort, P. A chemical–mineralogical classification of common plutonic rocks and associations. *Trans. R. Soc. Edinburgh: Earth Sci.* **1983**, *73*, 135–149.
39. Mao, Z.H., Cheng, Y.B., Liu, J.J., Yuan, S.D., Wu, S.H., Xiang, X.K., Luo, X.H. Geology and molybdenite Re–Os age of the Dahutang granite-related veinlets-disseminated tungsten ore field in the Jiangxin Province, China. *Ore Geol. Rev.* **2013**, *53*, 422–433.
40. Feng, C.Y, Zhang, D.Q., Xiang, X.K., Li, D.X., Qu, H.Y., Liu, J.N., Xiao, Y. Re-Os isotopic dating of molybdenite from the Dahutang tungsten deposit in northwestern Jiangxi Province and its geological implication. *Acta Petrol. Sin.* **2012**, *28*, 3858–3868.
41. Zhang, Z.H., Zhang, D., Wu, G.G., Luo, P., Chen, X.H., Di, Y.J., Lü, L.J. Re-Os isotopic age of molybdenite from the Meizikeng molybdenite deposit in Northern Jiangxi Province and its geological significance. *J. Jilin Univ. (Earth Sci. Edit.)* **2013**, *43*, 1851–1863.
42. Li, Q.L. "High-U effect" during SIMS zircon U-Pb dating. *Bull. Miner. Petrol. Geochem.* **2016**, *35*, 405–412.
43. Watson, E.B., Harrison, T.M. Zircon saturation revisited: Temperature and composition effects in a variety of crustal magma types. *Earth Planet. Sci. Lett.* **1983**, *64*, 295–304.
44. Miller, C.F., McDowell, S.M., Mapes, R.W. Hot and cold granites? Implications of zircon saturation temperatures and preservation of inheritance. *Geology* **2003**, *31*, 529–532.
45. Thompson, A.B. Partial melting of metavolcanics in amphibolite facies regional metamorphism. *J. Earth Sys. Sci.* **2001**, *110*, 287-291. DOI:10.1007/BF02702895.
46. Patin˜o Douce, A.E. What do experiments tell us about the relative contributions of crust and mantle to the origin of granitic magmas?. In *Understanding granities: Integrating new and classical techniques*; Castro, A., et al., eds.; Geological Society of London Special Publication: London, 1999, Volume 168, pp. 55–75.
47. Spear, F.S. Metamorphic phase equilibria and pressure-temperature-time paths. Mineralogical Society of America: Washington, DC, USA, 1995; pp.799.
48. Whalen, J., Currie, K., Chappell, B. A-type granites: geochemical characteristics, discrimination and petrogenesis. *Contrib. Mineral. Petrol.* **1987**, *95*, 407–419.
49. Taylor, R.P., Fallick, A.E. The evolution of fluorine-rich felsic magmas: source dichotomy, magmatic convergence and the origins of topaz granite. *Terra Nova* **1997**, *9*, 105–108.
50. Li, X.H., Li, Z.X., Li, W.X., Liu, Y., Yuan, C., Wei, G.J., Qi, C.S. U-Pb zircon, geochemical and Sr–Nd–Hf isotopic constraints on age and origin of Jurassic I- andA-type granites from central Guangdong, SE China: A major igneous event in response to foundering of a subducted flat-slab? *Lithos* **2007**, *96*, 186–204.
51. Sylvester, P.J., Liegeois, J.P. Post-collisional strongly peraluminous granites. *Lithos* **1998**, *45*, 29–44.
52. Simon, L., L´ecuyer, C. Continental recycling: the oxygen isotope point of view. Geochem. Geophys. *Geosys.* **2005**, *6*, 1–10.
53. Wei, W.F., Shen, N.P., Yan, B., Lai, C., Yang, J.H., Gao, W., Liang, F. Petrogenesis of ore-forming granites with implications for W–mineralization in the super-large Shimensi tungsten-dominated polymetallic deposit in northern Jiangxi Province, South China. *Ore Geol. Rev.* **2018**, *95*, 1123–1139.
54. Pearce, J.A. Source and settings of granitic rocks. *Episodes* **1996**, *19*,120–125.
55. Wang, X.L., Zhou, J.C., Griffin, W.L., Zhao, G.C., Yu, J.H., Qiu, J.S., Zhang, Y.J., Xing, G. F. Geochemical zonation across a Neoproterozoic orogenic belt: Isotopic evidence from granitoids and metasedimentary rocks of the Jiangnan orogen, China. *Precambram Res.* **2014**, *242*, 154–171.
56. Harris, N., Ayres,M., Massey, J. Geochemistry of graniticmelts produced during the incongruent melting of muscovite: implications for extraction of Himalayan leucogranite magmas. *J. Geophys. Res.* **1995**, *100*, 15767–15777.
57. Harris, N.B.W., Inger, S. Trace element modelling of pelite-derived granites. *Contrib. Mineral. Petrol.* 1992, *110*, 46–56.
58. Liu, Y.J., Ma, D.S. The geochemical studies of tungsten built in South China. *Sci.China B* **1982**, *10*, 939–950.
59. Lin, D.S. Tantalum-rich Granite Type Deposits in South China. Geological Publishing House: Beijing, China, 1996; pp. 147.

 doi:10.20944/preprints202510.0931.v1

60. Xu, J. W-bearing sedimentary formations and stratabound W-deposits in Jiangxi Province. *Geol. Prospect.* **1988**, *10*, 12–18.
61. Stepanov, A.S., Hermann, J. Fractionation of Nb and Ta by biotite and phengite: implications for the "missing Nb paradox". *Geology* **2013**, *41*, 303–306.
62. Černý, P., Belvin, P.L., Cuney, M., London, D. Granite-related ore deposits. *Economic Geology* **2005**,*100th Anniversary Volum*e, 337–370.
63. Bea, F., Fershtater, G., Corretgé, L.G. The geochemistry of phosphorus in granite rocks and the effect of aluminium. *Lithos* **1992**, *29*, 43–56.
64. Candela, P.A., Bouton, S.L. The influence of oxygen fugacity on tungsten and molybdenum partitioning between silicate melts and ilmenite. *Econ. Geol.* **1990**, *85*, 633–640.
65. Blevin, P.L. Redox and compositional parameters for interpreting the granitoid metallogeny of eastern Australia: implications for gold-rich ore systems. *Resour. Geol.* **2004**, *54*, 241–252.
66. Ishihara, S. The granitoids series and mineralization. *Econ. Geol*. **1981**, *75th Anniversary Volume*, 458–484.
67. Chen, T.H. On various features of the chemical composition of wolframites in a tungsten-tin deposit in Jiangxi Province. *J. Nanjing Univ. (Natural Sci.)* 1982, *1*, 133–145.
68. Tan, Y.J. Geochemical types of the vein wolframite deposits in the Nanling region. *Geochimica* **1982**, *2*, 155–161.
69. Zhao, B., Li, W.X., Cai, Y.J. Conditions of formation of wolframite, cassiterite, columbite, microlite and tapiolite and experimental studies on the variation of Nb and Ta in wolframite and cassiterite. *Geochimica* **1977**, *2*, 123–135.
70. Baker, T., Pollard, P.J., Mustard, R., Mark, G., Graham, J.L. A comparison of granite-related tin, tungsten, and gold-bismuth deposits: implications for exploration. *SEG Newslett*er **2005**, *61*, 5–17.
71. Blevin, P.L., Chappell, B.W. The role of magma sources, oxidation states and fractionation in determining the granite metallogeny of eastern Australia. *Trans. Royal Soc. Edinburgh* 1992, *83*, 305–316.
72. Sillitoe R.H. Porphyry Copper Systems. *Econ. Geol.* **2010**, *105*, 3–41.
73. Sun, W.D., Huang, R.F., Li H., Hu, Y.B., Zhang, C.C., Sun, S.J., Zhang, L.P., Ding, X., Li, C.Y., Zartman, R.E., Ling, M.X. Porphyry deposits and oxidized magmas. *Ore Geol. Rev.* **2015**, *65*, 97–131.
74. Linnen, R.L., Cuney, M. Granite-related rare-element deposits and experimental constraints on Ta-Nb-W-Sn-Zr-Hf mineralization. In *Rare-Element Geochemistry and Mineral Deposits*; Linnen, R.L., Samson, I.M., Eds.; Geological Association: Canada, 2008; Short Course Notes 17, pp. 45–67
75. Zaraisky, G.P., Korzhinskaya, V., and Kotova, N. Experimental studies of Ta_2O_5 and columbite–tantalite solubility in fluoride solutions from 300 to 550°C and 50 to100 Mpa. *Mineral. Petrol.* **2010**, *99*, 287–300. 10.1007/s00710 -010-0112-z.
76. Che, X.D., Linnen, R.L., Wang, R.C., Aseri, A., Thibault, Y. Tungsten solubility in evolved granitic melts: An evaluation of magmatic wolframite. *Geochim. Cosmochim. Acta* **2013**, *106*, 84–98.
77. Bali, E., Keppler, H., Audetat, A. The mobility of W and Mo in subduction zone fluids and the Mo–W–Th–U systematics of island arc magmas. *Earth Planet. Sci. Lett.* **2012**, *351*, 195–207.
78. Candela, P.A., Bouton, S.L. The influence of oxygen fugacity on tungsten and molybdenum partitioning between silicate melts and ilmenite. *Econ. Geol.* **1990**, *85*, 633–640.
79. Pollard, P.J. Geologic characteristics and genetic problems associated with the development of granite-hosted deposits of tantalum and niobium. In *Lanthanides, Tantalum and Niobium*; Möller, P., Cerny, P., Saupe, F., Eds.; Springer New York: Berlin Heidelberg, 1989; pp. 240–256.
80. Schwartz, M.O. Geochemical criteria for distinguishing magmatic and metasomatic albite-enrichment in granitoids: examples from the Ta–Li granite Yichun (China) and the Sn–W deposit Tikus (Indonesia). *Mineral. Deposita* **1992**, *27*, 101–108.
81. Helba, H., Trumbull, R.B., Morteani, G., Khalil, S.O., Arslan, A. Geochemical and petrographic studies of Ta mineralization in the Nuweibi albite granite complex, Eastern Desert, Egypt. *Miner. Deposita* **1997**, *32*, 164–179.
82. Wu, F., Sun, D., Huimin, L., Jahn, B., Wilds, S. A-type granites in northeastern China: age and geochemical constraints on their petrogenesis. *Chem. Geol.* 2002, *187*, 143–173.
83. Clarke, D.B. The mineralogy of peraluminous granites: a review. *Can. Mineral.* **1992**, *19*, 3–17.

 doi:10.20944/preprints202510.0931.v1

84. Shearer, C., Papike, J., Laul, J. Chemistry of potassium feldspars from three zoned pegmatites, Black Hills, South Dakota: implications concerning pegmatite evolution. *Geochem. Cosmochim. Acta* **1985**, *49*, 663–673.
85. Zaraisky, G.P., Aksyuk, A.M., Devyatova, V.N., Udoratina, O.V., Chevychelov, V.Y. The Zr/Hf ratio as a fractionation indicator of rare-metal granites. *Petrology* **2009**, *17*, 25–45.